Assimilating Space-Based Thermospheric Neutral Density (TND) Data Into the TIE-GCM Coupled Model During Periods With Low and High Solar Activity

Kosary, Mona; Farzaneh, Saeed; Schumacher, Maike; Forootan, Ehsan

Published in:
Space Weather

DOI (link to publication from Publisher):
10.1029/2023SW003811

Publication date:
2024

Document Version
Publisher's PDF, also known as Version of record

AGU ADVANCING EARTH AND SPACE SCIENCES

Space Weather®

RESEARCH ARTICLE
10.1029/2023SW003811

Key Points:

- Investigating the impact of covariance localization on the assimilation of Thermospheric Neutral Density data into TIE-GCM
- Assimilation the of TND data into TIE-GCM considerably improves the electron density forecasts in the ionosphere
- The agreement of the predicted TND and electron profiles with observations is better during the period of low solar than the high solar

Correspondence to:
S. Farzaneh,
farzaneh@ut.ac.ir

Citation:
Kosary, M., Farzaneh, S., Schumacher, M., & Forootan, E. (2024). Assimilating space-based thermospheric neutral density (TND) data into the TIE-GCM coupled model during periods with low and high solar activity. *Space Weather*, *22*, e2023SW003811. https://doi.org/10.1029/2023SW003811

Received 26 NOV 2023
Accepted 17 MAR 2024

Author Contributions:
Conceptualization: Saeed Farzaneh, Ehsan Forootan
Formal analysis: Mona Kosary
Methodology: Saeed Farzaneh, Maike Schumacher, Ehsan Forootan
Project administration: Ehsan Forootan
Supervision: Saeed Farzaneh, Ehsan Forootan
Validation: Mona Kosary, Maike Schumacher
Visualization: Mona Kosary
Writing – original draft: Mona Kosary
Writing – review & editing: Mona Kosary

Assimilating Space-Based Thermospheric Neutral Density (TND) Data Into the TIE-GCM Coupled Model During Periods With Low and High Solar Activity

Mona Kosary[1], Saeed Farzaneh[1], Maike Schumacher[2], and Ehsan Forootan[2]

[1]School of Surveying and Geospatial Engineering, College of Engineering, University of Tehran, Tehran, Iran, [2]Department of Planning, Geodesy Group, Aalborg University, Aalborg, Denmark

Abstract The global estimation of Thermospheric Neutral Density (TND) and electron density (Ne) on various altitudes are provided by upper atmosphere models, however, the quality of their forecasts needs to be improved. In this study, we present the impact of assimilating space-based TNDs, measured along Low Earth Orbit (LEO) mission, into the NCAR Thermosphere-Ionosphere-Electrodynamics General Circulation Model (TIE-GCM). In these experiments, the Ensemble Kalman Filter (EnKF) merger of the Data Assimilation Research Testbed (DART) community software is applied. To cover various space-based TND data and both low and high solar activity periods, we used the measurements of CHAMP (Challenging Minisatellite Payload) and Swarm-C as assimilated observations. The TND forecasts are then validated against independent TNDs of GRACE (Gravity Recovery and Climate Experiment mission) and Swarm-B, respectively. To introduce the impact of the thermosphere on estimating ionospheric parameters, the outputs of Ne are validated against the radio occultation data. The Data Assimilation (DA) results indicate that TIE-GCM overestimates (underestimates) TND and Ne during low (high) solar activity. Considerable improvements are found in forecasting TNDs after DA, that is, the Root Mean Squared Error (RMSE) is reduced by 79% and 51% during low and high solar activity periods, respectively. The reduction values for Ne are found to be 52.3% and 40.4%, respectively.

Plain Language Summary The atmosphere has different layers, like the thermosphere and ionosphere, which are important for satellite orbit prediction and communication. The empirical or physics-based models can be used to understand what's happening in these layers, but they aren't always accurate. In this study, the neutral density estimates along low earth orbit satellites have been integrated with the physics-based Thermosphere Ionosphere Electrodynamics General Circulation Model (TIE-GCM) through the Ensemble Kalman Filter (EnKF) Data Assimilation (DA) method. We found that using this data can help us make better predictions about the thermosphere and ionosphere variables. Our technique could be useful for predicting changes in the atmosphere in the short-term, which could be important for communication and navigation.

1. Introduction

With the development of satellite technology, the precise prediction of Low Earth Orbit (LEO) satellites and CubeSats have become increasingly important. These satellites fly in the altitude range of ~85–1,000 km, where the thermosphere and ionosphere are highly dynamic. The Thermospheric Neutral Density (hereinafter TND) at the satellites' altitudes will determine the drag force acting on their surface, and the speed at which they decelerate. Therefore, an accurate determination and propagation of the orbits of these objects (Doornbos, 2012; Krauss et al., 2018; Zesta & Huang, 2016) and their uncertainties depend on the quality of the TND predictions (Vallado, 2004; Vallado & Finkleman, 2014). However, estimating TND is challenging since the thermosphere-ionosphere system is highly influenced by solar irradiance, and it depends on the state of the neutral temperature and composition. Besides, external forces such as those related to the space weather events (Qian & Solomon, 2012; Qian et al., 2012; Solomon et al., 2011), as well as interactions between neutral molecules with charged particles considerably influence the thermospheric variability (Shim et al., 2014).

Various empirical and physics-based models have been developed to simulate and forecast TNDs and other features of the thermosphere in space and time. Empirical models such as the Naval Research Laboratory Mass Spectrometer and Incoherent Scatter radar Extended model (NRLMSISE-00, Picone et al., 2002), Drag Temperature Model (DTM, Bruinsma, 2015), Jacchia 1970 (J79, Jacchia, 1971), and Jacchia-Bowman 2008 (JB2008,

Bowman et al., 2008) are commonly used in the orbit determination applications. The Thermosphere Ionosphere Electrodynamics General Circulation Model (TIE-GCM, Roble & Ridley, 1994) and Coupled Thermosphere Ionosphere Plasmasphere electrodynamics (CTIPe, Millward et al., 2001) are among the frequently applied physics-based models that try to provide a full picture of interactions between the thermosphere and ionosphere parameters, such as the Total Electron Content (TEC), the three-dimensional electron density (Ne), and their evolution in time (fourth dimension) (Belehaki et al., 2009). The physical laws and principles such as the continuity, energy, and momentum equations are the main drivers of these models, which require the solution of partial differential equations (Fuller-Rowell & Rees, 1980; Roble & Ridley, 1994). Generally speaking, the energy and momentum are transferred from the lower to the upper thermosphere and ionosphere through the generation and propagation of waves. The neutral and ionized components of the upper thermosphere interact through several mechanisms including neutral winds, ion drag, chemical reactions, and electromagnetic coupling. These mechanisms affect the density and distribution of charged particles in the ionosphere, which are influenced by the neutral density. For example, neutral winds in the thermosphere drive ionospheric plasma circulation, while the ionosphere exerts a drag on neutral particles. Furthermore, chemical reactions in the upper thermosphere are affected by the density and temperature of the neutral and ionized species, which are in turn influenced by the neutral density. Finally, the ionosphere and thermosphere are electrically coupled, with changes in the ionosphere electric fields and currents affecting the neutral winds and neutral density distribution. These interactions make the thermosphere-ionosphere a coupled system. The physics-based models require primary state information, boundary conditions, and a proper set of parameters to be able to run and generate meaningful outputs (Qian et al., 2014; Richmond et al., 1992).

Previous studies have shown that the now-casting and forecasting capabilities of current empirical and physics-based models are limited (i.e., one can find periods with over and underestimations) due to the lack of information about external drivers, simplified model structures, and the sensitivity to the calibration period (Forootan et al., 2020, 2022; Kosary et al., 2022; Miyoshi et al., 2011; Palmroth et al., 2021; Vielberg et al., 2018). Thus, further enhancements, by taking advantage of the thermosphere-ionosphere observations, can improve characterizing and predicting thermosphere-ionosphere variability as accurately and efficiently as possible. This view has been followed by implementing the state-of-the-art of Data Assimilation (DA) as a powerful tool for merging available observations and models in space weather and geodetic applications (e.g., Hajj et al., 2004; Hsu et al., 2014; Khattatov et al., 2005; Lee et al., 2012; Matsuo & Araujo-Pradere, 2011; Pi et al., 2003; Scherliess et al., 2004, 2006, 2009; C. Wang et al., 2004; W. Wang et al., 2004).

The DA techniques can provide updates to the initial model states, which can enhance the forecasting skills through combining the physics-based background model with observations (Baker & Daley, 2000). Considerable efforts have already been taken to improve the accuracy of physics-based models by implementing DA for the thermospheric temperature (e.g., Cantrall et al., 2019; Ruan et al., 2018), Thermospheric Neutral Density (TND, e.g., Forootan et al., 2020, 2022; Sutton, 2018; Weimer et al., 2020), neutral compositions (e.g., M. V. Codrescu et al., 2004; P. M. Mehta et al., 2019; J. Yue et al., 2019), and wind patterns (e.g., Cierpik et al., 2003; Lomidze et al., 2015). There have been other studies that indirectly specified thermosphere properties (such as neutral winds, mass density, and temperature) by assimilating the ionospheric measurements into coupled models (e.g., Aa et al., 2016; G. Bust & Immel, 2020; G. S. Bust et al., 2004; Chen et al., 2016; Datta-Barua et al., 2013; Forsythe, Azeem, Blay, Crowley, Gasperini, et al., 2021; Forsythe, Azeem, Blay, Crowley, Makarevich, & Wu, 2021; He et al., 2020; Kodikara et al., 2021; Lee et al., 2012; Lin et al., 2015; N. M. Pedatella et al., 2020). In most of these studies, the physics-based general circulation models are used because they are suitable for understanding the complex behavior of terrestrial atmosphere in different spatial and temporal scales (e.g., Emmert, 2015; Fesen et al., 2002; Huba & Sazykin, 2014; P. Mehta & Linares, 2017; Qian & Solomon, 2012; Sutton, 2018). This choice will also be considered in this study.

Though various thermosphere and ionosphere data sets are proposed for improving models through DA frameworks, the along-track TND estimates derived from the drag acceleration analysis of Low Earth Orbit (LEO) satellites can be considered as a one of reliable data source that is available by launching various LEO missions. For example, the Challenging Minisatellite Payload (CHAMP, 2000–2010, Reigber et al., 2002), the Gravity Recovery and Climate Experiment (GRACE, 2002–2017, Tapley et al., 2004) and its follow-on mission (GRACE-FO, launched in 2018, Flechtner et al., 2014), Gravity field and steady-state Ocean Circulation Explorer (GOCE, 2009–2013, Albertella et al., 2002) and the European Space Agency (ESA)'s Swarm mission (Swarm A, B, and C launched in 2013, Visser et al., 2013), which are equipped with the accelerometer sensor to measure non-

gravitational forces. Various data providers, for example, Delft Technical University ((Siemes et al., 2023; Van Den IJssel et al., 2020)), European Space Agency (https://earth.esa.int), P. M. Mehta et al. (2017), and Vielberg et al. (2021) freely share their TND estimates. However, since these measurements are only available along the orbits of LEO missions, their usage for analyzing global and multi-level TND (and its composition) variations is a research in progress (Forootan et al., 2022). Prior to this study, Matsuo et al. (2013) applied TND along CHAMP orbits for tuning the TIE-GCM model. Sutton (2018) proposed a new data assimilation technique based on the iterative model reinitialization to update and estimate a time-series of effective solar and geophysical drivers using the TND measurements of CHAMP in 2003. The new technique decreased the Root Mean Squared Error (RMSE) of TIE-GCM TND estimates as shown by Ren and Lei (2020). S. M. Codrescu et al. (2018) suggested a DA approach to improve the CTIPe model by ingesting CHAMP TND measurements. The validation was performed with CHAMP and GRACE measurements during the solar minimum period.

General circulation model equations are nonlinear, thus, inferring the state variables from (indirect) observations of TNDs (or any other observed variables) is an inverse problem, which is computationally unstable. To mitigate the non-linearity problem, the Ensemble Kalman Filter (EnKF) technique (e.g., Evensen, 2009) is applied as a merger through the Data Assimilation Research Testbed (J. Anderson et al., 2009, DART) implementation. One of the limitations of the EnKF-based DA is that the covariance matrices, which are needed to weight the model outputs and observations in the DA's merging procedure, are replaced with the sample covariance matrices (J. Anderson, 2001). To make the computational load affordable, the ensemble size has been selected to be lower than the dimension of the model states. As a result, the sample covariance matrices are rank-deficient, which can contribute to the sampling error and the long-range spurious correlations in the sample covariance matrices (Hamill et al., 2001; Houtekamer & Zhang, 2016; Lorenc, 2003). These spurious correlations will likely introduce incorrect updates to the state vectors by an observation that is physically only remotely connected to the variables that we wish to change within the DA. This issue is often mitigated by applying a localization technique (Bergemann & Reich, 2010; Farchi & Bocquet, 2019; Zhu et al., 2011), whereas the Schur product, which seeks to reduce spurious correlations using a weighting function with pre-defined cut-off radius, is applied to disregard the long-distance correlations. In this study, we will assess the role of the cut-off radius in the DART implementation of EnKF (hereinafter DART-EnKF) for estimating the model states during the analysis and forecast steps.

Another issue that exists for the DA of general circulation models is the relation between geometrical height and atmospheric pressure (i.e., model level). The calculation of geometric height in TIE-GCM is based on an empirical equation that relates the spatially varying gravity acceleration with temperature and the neutral density composition (Qian et al., 2014). The vertical coordinates system in TIE-GCM is defined based on the atmospheric pressure levels. Assimilating new observations, such as TNDs, might expand the vertical distance between consecutive pressure layers, therefore, leading to a change in the geometric height of the boundary layers. In other words, the relationship between the geometric heights and pressure levels will change after implementing DA. To address this problem, we determine geometric heights after DA.

The objectives and investigations of this paper are innovative and complement previous studies by (a) demonstrating how well global thermospheric and ionospheric state variables can be improved by assimilating LEO TNDs into the TIE-GCM during periods with low ($F_{10.7} \sim 70$ SFU) and high ($F_{10.7} \sim 140$ SFU) solar activity; (b) assessing three sets of real TND estimates from CHAMP (4–8 March 2008), CHAMP (13–16 August 2004) and Swarm-C (4–8 February 2015) missions as observation of the DA; (c) validating the analysis and forecast steps with GRACE and Swarm-B TND (i.e., these data were not introduced during the DA procedure); (d) assessing the impact of TND DA on the forecasting electron density in the ionosphere by validating the results with FORMOSAT-3/COSMIC (F3/C) electron density profiles; and (e) exploring the impact of the TND DA in space and time, and providing detailed statistics of the performance during both analysis and forecast steps.

2. Model and Data

2.1. TIE-GCM

The fully coupled TIE-GCM version 2.0 model (released on 21 March 2016), which is a three-dimensional physics-based global model of the thermosphere-ionosphere is used in this study. TIE-GCM self-consistently solves the coupled nonlinear momentum, energy, and continuity equations for neutral and ion species based on the finite differencing technique in hydrostatic pressure coordinates (Maute, 2017; Qian et al., 2014; Richmond et al., 1992; Roble & Ridley, 1994). The outputs of TIE-GCM include the simulations of global distribution of the

neutral wind circulation, temperature, electrodynamics, and compositions of the upper atmosphere and ionosphere. The horizontal resolution of TIE-GCM used for this study is 5° × 5° in longitude and latitude, and the vertical resolution is two levels per scale height. We used 29 constant pressure surface layers that extend from ~97 to 600 km in altitude. The limit of the upper boundary primarily depends on the level of solar activity. In TIE-GCM, the high latitude ion convection is generated using one of the empirical models. The first is the Heelis (Heelis et al., 1982), which is driven by the Kp index to estimate the hemisphere power (*HP*) and cross-polar-cap potential drop (*CP*), which are required to determine the high latitude energy and momentum. The latter is the Weimer empirical model, which is parameterized by the interplanetary magnetic field (IMF) strength and direction, as well as the solar wind speed and density (Weimer, 2005). In the model run presented here, TIE-GCM uses the F10.7 index ($F_{10.7}$, Heelis empirical model and atmospheric tides as inputs. The *HP* and *CP* can be determined from *Kp* as (Zhang & Paxton, 2008):

$$CP = 15.0 + 15.0Kp + 0.8Kp^2, \tag{1}$$

$$HP = \begin{cases} 16.82 \quad \exp(0.32 \times \mathrm{Kp}) - 4.86, & \text{if } Kp \le 7 \\ 153.13 + 73.435 \quad (\mathrm{Kp} - 7), & \text{if } Kp > 7. \end{cases} \tag{2}$$

In the model runs presented here, migrating diurnal and semi-diurnal tides at the lower boundary are specified using the global-scale wave model (Hagan et al., 2001). Also, the model adds day-of-year dependent perturbations to the advective and diffusive transport via the eddy diffusion coefficient as described in Qian et al. (2009). The complete model description can be found on the National Center for Atmospheric Research (NCAR) website (http://www.hao.ucar.edu/modeling/tgcm/tie.php).

2.2. Space-Borne Thermospheric Neutral Density (TND) Data

The accelerometer-based TNDs along CHAMP during two periods (4–8 March 2008) and (13–16 August 2004), and Precise Orbit Determination (POD) based TNDs along Swarm-C (4–8 February 2015) orbits are used as observation in the DA experiments. For validation, the TND data along the GRACE and Swarm-B orbits are used. All data are derived from the TU Delft data set (Siemes et al., 2023; Van Den IJssel et al., 2020). The reason for using POD-based TNDs along Swarm missions is that the accelerometer observations of Swarm contain jumps (Visser et al., 2013). Further information about each mission is provided in Data Availability Statement.

Since the density estimates from various satellite missions may require inter-calibration (López López et al., 2017), we perform a distribution-based inter-calibration approach along validation TNDs as (P. Mehta & Linares, 2018):

$$\rho_{cal} = SF\rho_{raw}, \tag{3}$$

where ρ_{cal} contains calibrated TNDs, ρ_{raw} indicates the measured ones, and finally *SF* represent a scale factor to be determined. The value of *SF* is calculated by dividing the average of monthly observation to the model ratio of DA to the validation TNDs as $SF = mean(TND_{DA}/tiegcmTND_{DA})/mean(TND_{Validate}/tiegcmTND_{Validate})$.

In this study, the TIE-GCM model provides simulations of the thermosphere-ionosphere system over a wide range of altitudes. However, during periods of low solar activity, the TIE-GCM simulations do not cover altitudes as high as those observed by the GRACE satellite mission during 4–8 March 2008. To facilitate comparison between the TIE-GCM and data assimilation simulations and the GRACE observations, we transformed the GRACE-TNDs from their original altitude (~487 km) to a common altitude of 400 km such as previous study (Fernandez-Gomez et al., 2022). For this purpose, a height-dependent function based on the NRLMSISE00 model (Picone et al., 2002) is applied to transform the TND estimates of various altitudes to their equivalent values at 400 km as:

$$\rho(400) = \rho(h)\ \frac{\rho_N(400)}{\rho_N(h)}, \tag{4}$$

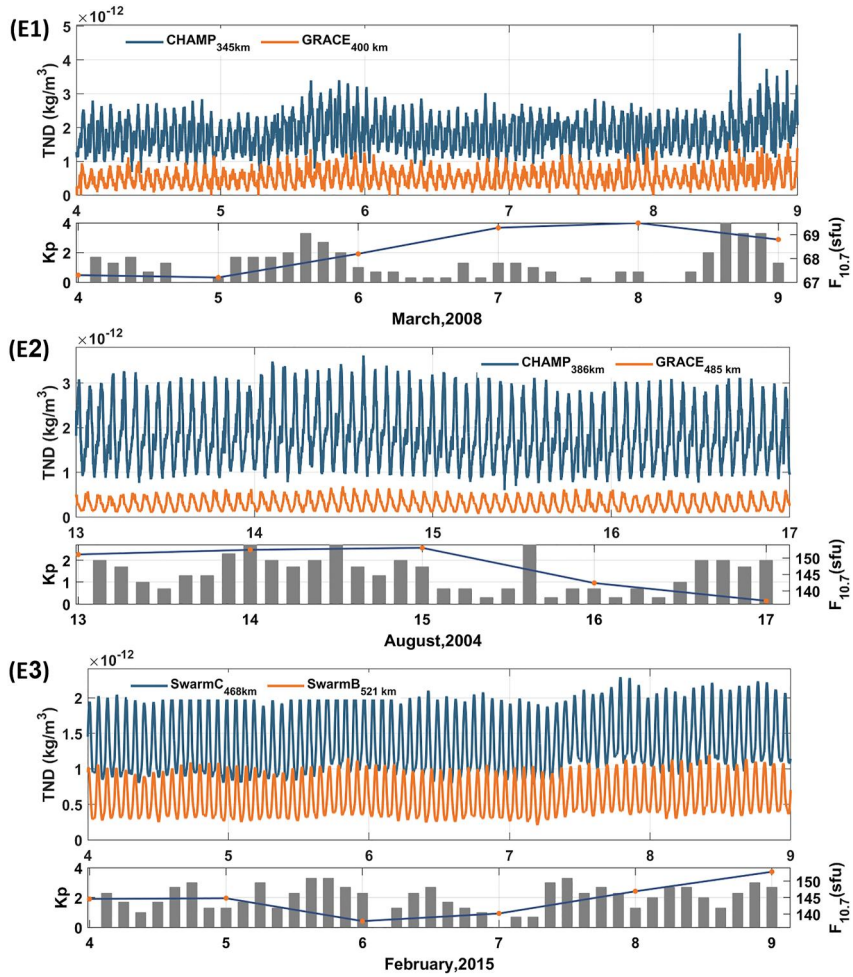

Figure 1. An overview of the thermospheric neutral density data used in this study: From top to bottom for three experiments: (E1) Top: TNDs from CHAMP at their altitudes and GRACE at 400 km, Bottom: Space weather conditions for the experiment 1 during March 4^{th}–8^{th}, 2008, (E2) Top: TNDs from CHAMP and GRACE at their altitudes, Bottom: Space weather conditions for the experiment 2 during August 13^{th}–16^{th}, 2004, (E3) Top: TNDs of Swarm-C and Swarm-B at their original altitudes, Bottom: Space weather conditions for the experiment 3 during February 4^{th}–8^{th}, 2015. For the bottom plots, the solar activity ($F_{10.7}$) and 3-hr geomagnetic activity (Kp) indices are shown. The range of changes in the $F_{10.7}$ index is 5 (SFU), 20 (SFU), and 20 (SFU) during E1, E2, and E3 experiments, respectively. Here, the inter-calibration of Section 2.2 is applied to the TND values along validation missions.

where $\rho(h)$ is the observed density at the altitude h, while $\rho_N(400)$ and $\rho_N(h)$ stand for the TNDs of NRLMSISE-00 at the altitude of 400 and h km, respectively.

2.3. Definition of the DA Experiments

Three experiments are investigated to assess the capability of the DA to tune the TIE-GCM model using real TND data, where in **E1**, we assimilate CHAMP-TNDs during low solar activity (4–8 March 2008, $F_{10.7} \sim 70$ SFU);**E2**, The CHAMP-TNDs during high solar activity (13–16 August 2004, $F_{10.7} \sim 145$ SFU) are tuned to the model; and in **E3**, Swarm-C-TNDs during high solar activity (4–8 February 2015, $F_{10.7} \sim 140$ SFU) are applied.

Figure 1 provides an overview of the data used in this study. Panel (E1) contains two plots in which the top plot represents the time series of along-track TND estimates derived from CHAMP and GRACE at their original altitude and at the common altitude of 400 km (during E1), respectively, and the bottom refers to the variation of solar and planetary geomagnetic activity represented by $F_{10.7}$ from https://www.spaceweather.gc.ca/forecast-prevision/solar-solaire/solarflux/sx-en.php and Kp indices from https://doi.org/10.5880/Kp.0001. Panels (E2) and (E3) are similar to that of E1, but correspond to CHAMP and GRACE, and Swarm-C and Swarm-B, during E2

and E3, respectively. Considering E1, E2, and E3 provides an opportunity to compare the TND DA results with different missions at two different levels of solar activity.

2.4. Electron Density Profile From Radio Occultation Measurements

The electron density (Ne) profiles from the joint USA-Taiwan Constellation Observing System for Meteorology, Ionosphere, and Climate/Formosa Satellite 3 (COSMIC/FORMOSAT-3; hereinafter called COSMIC) mission are employed to validate the ionospheric outputs of the TND DA experiments. COSMIC contains a constellation system of six micro-satellites that were launched on 15 April 2006, and reached 800 km around December 2007. Each satellite carries four receivers, which can receive GNSS signals that are transmitted through the ionosphere. Electron density (Ne) profiles are retrieved from the phase differences under the assumption of spherical symmetry of the electron density distribution (Liou et al., 2007). In this study, we used the second-level "ionPrf" data products, which are available from http://www.cosmic.ucar.edu. The accuracy of COSMIC estimates is generally about 10^4–10^5 cm^{-3}, see the COSMIC program office website (http://cdaac-www.cosmic.ucar.edu/cdaac/products.html). Before validating the DART/TIE-GCM with RO data, it is necessary to perform quality control tests on individual profiles, which are applied following (Lei et al., 2007; Yang et al., 2009) and Yang et al. (2009).

3. Materials and Methods

3.1. EnKF Data Assimilation (DA) System

The Data Assimilation Research Testbed (DART) community software (J. Anderson et al., 2009) is used in this study to tune the TIE-GCM using TNDs as observation. DART is open-source software that facilitates the assimilation of different kinds of observations into models using a variety of filtering algorithms (Burgers et al., 1998; J. Anderson, 2001; J. Anderson et al., 2009). The updated TIE-GCM model after the DA is named here "DART/TIE-GCM."

The EnKF is applied as a merger to deal with the nonlinear equations of TIE-GCM (Evensen, 2003). In this study, the estimation of statistics (means and covariance), to weight model outputs and measurements, is derived by ensemble generation and empirical covariances (e.g., J. Anderson et al., 2009). The EnKF algorithm is recursive and consists of the "analysis" and the "forecast" steps. In the analysis step, the ensemble member of posterior state variables is estimated and updated through the cross covariances between the observations and prior state variables. In the forecast step, the posterior ensemble member is propagated forward in time with the TIE-GCM model equations for one assimilation cycle to solve the coupling processes and to produce priory ensembles for the next assimilation window.

To eliminate spurious correlations (Houtekamer & Zhang, 2016) that might negatively impact achieving correct updates, we apply the distance-based localization function following Gaspari and Cohn (1999). This is multiplied by the covariance matrix built between the prior state vector and observations. The EnKF-based DA updates the m-dimensional state vector X_k of TIE-GCM at time t_k through minimizing the following cost function:

$$J(\mathbf{X}_k) = \frac{1}{2}\left[\mathbf{X}_k - \bar{\mathbf{X}}_k^b\right]^T \left(\mathbf{P}_k^b\right)^{-1} \left[\mathbf{X}_k - \bar{\mathbf{X}}_k^b\right] + \frac{1}{2}\left[\mathbf{H}_k\mathbf{X}_k^b - \mathbf{Y}_k^o\right]^T \mathbf{R}_k^{-1} \left(\mathbf{H}_k\mathbf{X}_k^b - \mathbf{Y}_k^o\right), \quad (5)$$

where $\mathbf{X}_k^b$ denotes the background, that is, estimates of the state vector at time t_k and its associated covariance matrix $\mathbf{P}_{k,m\times m}^b$ from the ensemble of model forecasts. The model prediction of the state vector $\mathbf{X}_k^b$ from time t_{k-1} to t_k can be written as $\mathbf{X}_k = f(\mathbf{X}_{k-1})$ in which the nonlinear dynamics f is implemented through the model simulation code. In Equation 5, $\mathbf{Y}_k^o$ is the ensemble of n-dimensional vector of observations at time t_k, which can be related to $\mathbf{X}_k$ through the linear (or linearized) observation equation $\mathbf{Y}_k^b = \mathbf{H}_{k,n\times m}\mathbf{X}_k + \epsilon_k$, where $\mathbf{H}_k$ is design matrix and ϵ_k is the observation error vector.

The analysis state estimates ($\mathbf{X}^a$) are obtained while taking into account the measurements and the cross-correlations with the model states as:

$$\mathbf{X}_k^a = \mathbf{X}_k^b + \mathbf{K}\left(\mathbf{Y}_k^o - \mathbf{H}_k\mathbf{X}^{b_k}\right), \quad (6)$$

where $\mathbf{K}$ is the Kalman gain that is defined as:

$$\mathbf{K} = \left(\mathbf{C}_{loc1} \circ \left(\mathbf{H}_k \mathbf{P}_k^b\right)\right)^{\mathrm{T}} \left(\mathbf{C}_{loc2} \circ \left(\mathbf{H}_k \mathbf{P}_k^b \mathbf{H}_k^{\mathrm{T}}\right) + \mathbf{R}_k\right)^{-1}. \tag{7}$$

In Equation 7, $\mathbf{C}_{loc1,n\times m}$ and $\mathbf{C}_{loc2,n\times n}$ (n = number of observations and m = number of the model states included in the DA) are localization matrices suggested by Gaspari and Cohn (1999) with $\circ$ denoting the Schur product (element-wise) of matrices with identical size. The impact of the localization is shown in Section 4.1.

3.2. Configuring the TND Data Assimilation (TND DA)

3.2.1. Initialization of the Model Ensembles

The model ensembles used in the EnKF are generated by perturbing three model parameters: the solar index $F_{10.7}$, auroral hemispheric power *HP* Equation 2, and cross-tail potential drop *CP* Equation 1. The mean values of these model drivers are obtained from the corresponding observations of $F_{10.7}$, and the 3-hourly planetary index *Kp*. The ensemble simulation during low (high) solar activity is initialized following the recommendations in (Hsu et al., 2014, 2018; Kodikara et al., 2021) by Gaussian distributions with the mean value of $F_{10.7}$, *HP*, and *CP* set to 68 (150) SFU, 19 (25) GW, and 34 (45) kV, and with the standard deviation set to 10 (10) SFU, 2 (2.5) GW, and 3 (4.5) kV, respectively. Note that instead of employing the realistic variation of drivers in this study, these constant values with their spread are used to test the forecast performance of the assimilation system when the true drivers are not known. In addition, before the DA procedure, the model ensembles need a spin-up to arrive at a physically consistent state with perturbed drivers. The spin-up time for the model ensemble members is chosen to be 15 days, similar to Kodikara et al. (2021).

3.2.2. Specifications of the DART Implementation for the TND DA

The configuration of DART to implement the TND DA is selected to be as:

- Following the recommendation in Hsu et al. (2018), to achieve useful covariance estimations, the ensemble size is chosen to be 90 for each experiment.
- The Gaspari and Cohn (GC) correlation function (Gaspari & Cohn, 1999) is chosen for the localization, which is a distance-based function that gradually changes from one to zero with increasing the distance. Three experiments with different horizontal half-width values of 0.2, 1, and 3 radians were tested to find an optimum cutoff. No vertical localization is applied for the DA to introduce the impact of TNDs to all model levels. The GC correlation function between the *i*th observation and the *j*th grid point of the model state is estimated as:

$$\mathbf{C}_{i,j} = \begin{cases} -\frac{1}{4}\left(\frac{|r|}{c}\right)^5 + \frac{1}{2}\left(\frac{|r|}{c}\right)^4 + \frac{5}{8}\left(\frac{|r|}{c}\right)^3 - \frac{5}{3}\left(\frac{|r|}{c}\right)^2 + 1, & 0 \le |r| \le c \\ \frac{1}{12}\left(\frac{|r|}{c}\right)^5 - \frac{1}{2}\left(\frac{|r|}{c}\right)^4 + \frac{5}{8}\left(\frac{|r|}{c}\right)^3 + \frac{5}{3}\left(\frac{|r|}{c}\right)^2 - 5\left(\frac{|r|}{c}\right) + 4 - \frac{2}{3}\left(\frac{c}{|r|}\right), & c \le |r| \le 2c \\ 0, & |r| \ge 2c \end{cases} \tag{8}$$

where $|r|$ is the horizontal distance between the model grid point and the location of observation, and c is the cut-off radius.

- The assimilation window is 1,800 s—centered at the current model time. The neutral density observations within 15 min before and after a given model time are assimilated for each assimilation cycle. It is worth mentioning that we empirically chose various DA window (with 10, 30 min, 1 hr, and 1.5 hr) and the results of the different window in the forecasting step can be found in Section 4.1.
- The state vector to be updated is composed of:

$$\mathbf{X} = \left[\Psi^{Tn}; \Psi^{O2}; \Psi^{O}; \Psi^{U}; \Psi^{V}; \Psi^{Ne}\right], \tag{9}$$

where *Tn*, *O*, *O2*, *U*, *V*, and *Ne* represent the neutral temperature (*K*), mass mixing ratio of atomic oxygen (mmr), mixing ratio of molecular oxygen, zonal (east-west) wind ($\mathrm{m.s^{-1}}$), meridional (north-south) wind ($\mathrm{m.s^{-1}}$),and

Table 1
A Summary of the Statistical Measures Derived From TIE-GCM and DART/TIE-GCM Prior Outputs

Model	RMSE (kg/m^3)	Nash	Memory	Time (Hour)
Original TIE-GCM	3.61×10^{-13}	−2.95	–	–
DART/TIE-GCM (DA window = 10 min)	1.27×10^{-13}	0.58	3.6 (GB)	6.5
DART/TIE-GCM (DA window = 30 min)	1.28×10^{-13}	0.57	1.2 (GB)	5.4
DART/TIE-GCM (DA window = 60 min)	1.30×10^{-13}	0.56	630 (MB)	4.5
DART/TIE-GCM (DA window = 90 min)	1.39×10^{-13}	0.50	450 (MB)	3

Note. Here CHAMP-TNDs are used as observation within DA, and the results are evaluated with those of the $GRACE_{400}$ TNDs during 4 March 2008.

electron number density (cm^{-3}), respectively. The full vector of these physical variables discretized on the horizontal and vertical resolution of the model is represented by Ψ. It is noted that the vertical levels in TIE-GCM are defined based on the log pressure and geopotential height Zp. By changing the composition and temperature of model states, through the TND DA, the geometrical heights Zg of the geopotential levels change. The new geometrical heights can be estimated using an empirical formulation can be found in Qian et al. (2014).

3.3. Evaluation Metrics

Various evaluation measures are applied to examine the performance of the original and data assimilation procedure in analysis and forecast steps compared to the observation, including "Bias" (Equation B1),"Relative Error" (RE, Equation B2), "$Bias_{ratio}$" (Equation B3), "Root Mean Squared of Error" (RMSE, Equation B4), "Improvement" (Equation B5), "Average of Absolute Percentage Deviation" (AAPD, Equation B6), "Nash-Sutcliffe model Efficiency Coefficient" (Nash, Equation B7), "STD_{ratio}" (Equation B8), and "Correlation Coefficients" (CCs, Equation B9). For details, see Appendix A. It is noted that in this study, we compute each metrics among each experiment period.

4. Results

In what follows, the outputs derived from DART/TIE-GCM are investigated. In Section 4.1, the effect of the horizontal cut-off parameter is assessed. Then, the TND estimates of TIE-GCM and DART/TIE-GCM are validated in the analysis and forecast modes (Sections 4.2 and 4.3). Three experiments with different levels of solar activity are applied to understand whether the DA is effective in different periods. In Section 4.4, the dominant spatial and temporal variability of TND and electron density estimates are extracted from the forecast modes. Finally, in Section 4.5, the profiles of electron density from original TIE-GCM and DART/TIE-GCM are evaluated against RO observations.

4.1. Impact of the Data Assimilation Window and Horizontal Localization

In this part, we investigate the impact of different data assimilation windows on TND forecasting along the validation mission. We select 10, 30, 60, and 90 min as data assimilation windows for this purpose, and the numerical results along $GRACE_{400}$ during 4th March 2008 are provided in Table 1. According to these statistical criteria, 10 min of cycling yields a lower RMSE compared to the other windows in the forecast steps for 4 March 2008, from 00:00 UT to 23:00 UT. Although 10-min assimilation windows can yield slightly better prediction accuracy, this improvement is not cost-effective compared to the additional computational time and memory required (for a system with 4 cores and 16 GB RAM configuration). So, we took into account the balance between forecast accuracy and computational efficiency and we decided to use a 30-min assimilation window for assimilating TNDs into the TIE-GCM model for short-term forecasting. We believe that our choice of assimilation window length was suitable for our specific application and yielded meaningful outcomes. However, this choice of assimilation window length can be different in ionosphere data assimilation studies (Chen et al., 2016).

In order to find the impact of the cut-off parameter on forecasting TND, three different cut-offs of 0.2, 1, and 3 radians with no vertical localization are employed during the DA implementations. Figure 2 shows how the corresponding global GC correlation functions can affect the model around an arbitrary point, for example, with

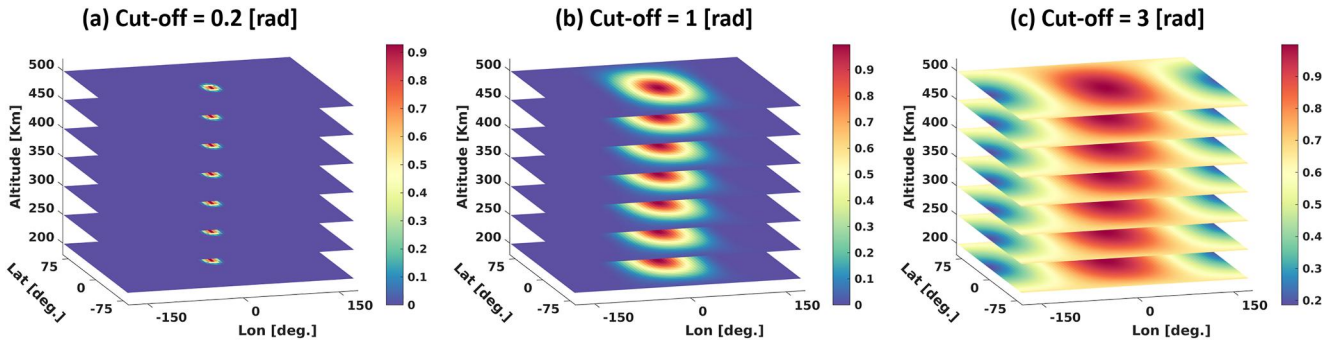

Figure 2. The localization maps from the Gaspari–Cohn (GC) function (Gaspari & Cohn, 1999). These results correspond to an arbitrary selected position with latitude = 0° and longitude = 0°. From left to right, plots correspond to the horizontal cut-off of (a) 0.2 radian, (b) 1 radian, and (c) 3 radian.

latitude 0° and longitude 0°. Selecting 0.2 in this location corresponds to 2548.4 km, where for 1 and 3, it is 12,742, and 38,226 km, respectively.

The TND estimates along the CHAMP orbits during 4 March 2008 are considered as observations to test the three cut-off values. Observations along the $GRACE_{400}$ are used for validation. The results demonstrate that the RMSE between original TIE-GCM and $GRACE_{400}$ TNDs during 1 day is reduced by 69%, 80%, and 84% after implementing DART/TIE-GCM with the horizontal cut-off of 0.2, 1 and 3 radians, respectively. Therefore, we can show that the three values of cut-off can reduce the RMSE, but the numerical values indicate that the selection of three radians provides better thermosphere outputs compared to the independent TND measurements. In addition, for comparison, the bias, RMSE as well as the Nash coefficient between $GRACE_{400}$ TNDs and those TIE-GCM and DART/TIE-GCM outputs in the forecasting mode are presented in Table 2. These numerical results indicate that the use of bigger cutoff value results in better statistical measures. Therefore, the cutoff of three is used for the experiments of the following sections, and we will ensure that this almost global updating scheme does not harm the physics of the model that could harm the prediction of ionosphere variables. Although the TND can be predicted accurately using this cut-off value, updating more state vectors can increase the computation time.

4.2. Impact of the TND DA on Reducing Biases During the E1 Experiment With Low Solar Activity

To evaluate DART/TIE-GCM through the E1, E2, and E3 experiments with low and high solar activity (Figure 1), we determine the *Bias* (Equation B1) against the assimilated observations of E1 (CHAMP), E2 (CHAMP) and E3 (Swarm-C). Figure 3 shows the impact of DART/TIE-GCM on the CHAMP-TNDs measurements during E1. The top plot represents the orbit-averaged TNDs derived from TIE-GCM (gray line), the analysis phase (blue line), the forecast (red line) as well as CHAMP estimates are shown by the green line. The plots show an overall agreement between the analysis and forecast steps, and CHAMP TNDs, that is, biases between TIE-GCM, analysis and forecasts phases compared to the CHAMP TND estimates are found to be -1.1×10^{-12}, 6.9×10^{-14}, and 5.5×10^{-14}, while the correlation coefficients are 0.85, 0.87, and 0.83.

The plot in the middle represents a zoom of the results on 5 March 2008. The plot shows that the TNDs of both analysis and forecast steps catch the 1.5 hourly peaks, where both timing and magnitude are found to be correctly

Table 2
A Summary of the Statistical Measures Derived From TIE-GCM and DART/TIE-GCM Prior Outputs

Model	Bias (kg/m^3)	RMSE (kg/m^3)	Nash
Original TIE-GCM	3.43×10^{-13}	3.61×10^{-13}	−2.95
DART/TIE-GCM (cut-off = 0.2 rad)	0.9×10^{-13}	1.12×10^{-13}	−0.21
DART/TIE-GCM (cut-off = 1 rad)	0.37×10^{-13}	0.71×10^{-13}	0.50
DART/TIE-GCM (cut-off = 3 rad)	0.17×10^{-13}	0.58×10^{-13}	0.67

Note. Here CHAMP-TNDs are used as observation within DA, and the results are evaluated with those of the $GRACE_{400}$ TNDs during 4 March 2008.

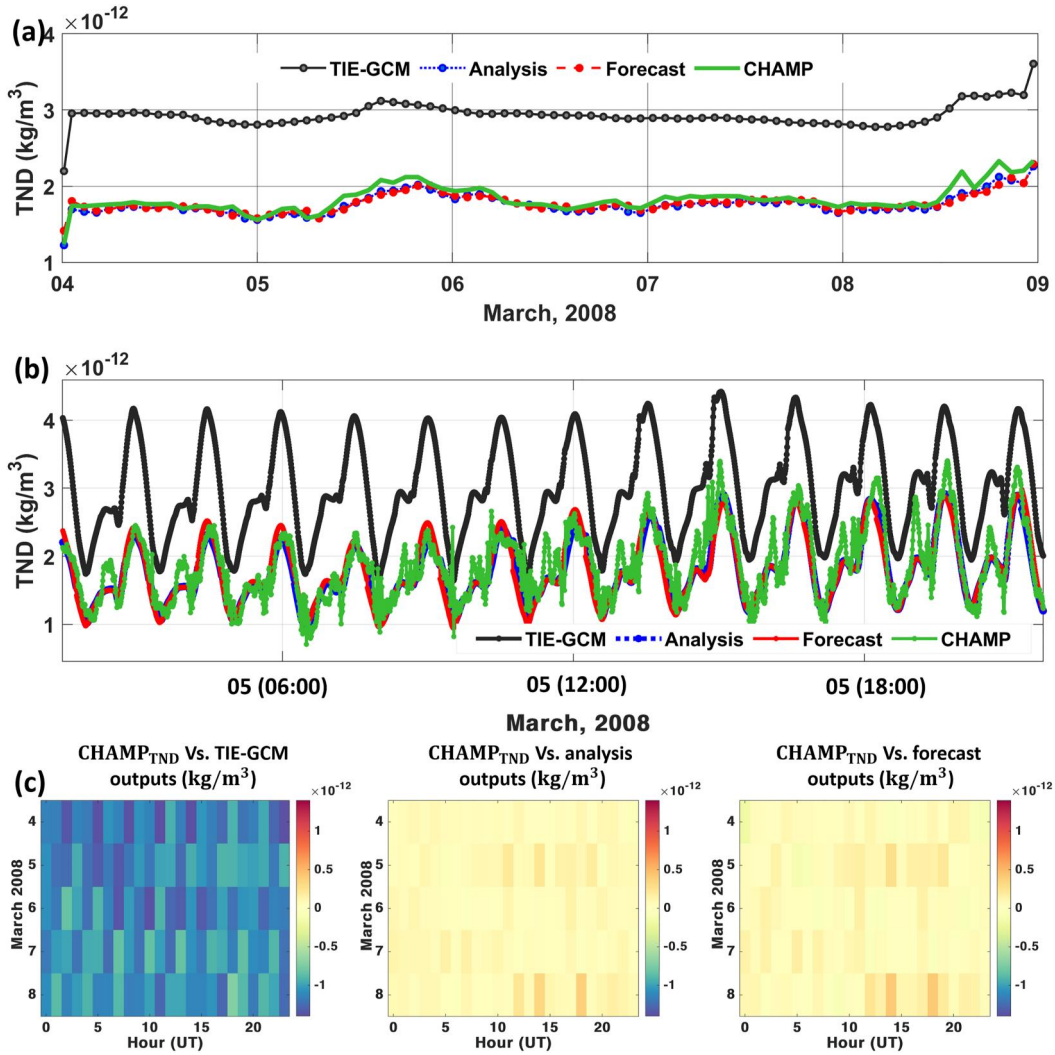

Figure 3. Assessing model biases before and after the TND DA: (a) orbit-averaged TNDs from TIE-GCM, DART/TIE-GCM outputs in the analysis and forecast modes, as well as TNDs along the orbit of CHAMP within the E1 experiment (March 4^{th}–8^{th}, 2008); (b) time-series of TND during 24 hr of 5 March 2008; and (c) a summary of biases (from Equation B1) between the observed and simulated TNDs in the analysis and forecast modes. The results during the E1 experiment are shown as a function of hour and day. Here, the DART/TIE-GCM is processed using CHAMP-TNDs as assimilation observation.

represented. Especially, one can see that the magnitude of the peaks (i.e., the ratio between the mean of TNDs after and before 12 hr) after ~12 hr has been increased ~69.1% and these changes are well represented in the plots. Figure 3(bottom) summarizes the one hourly biases during March $4th - 8th$, 2008, where on average we found a reduction from -1.10×10^{-12} to 6.92×10^{-14} and 5.77×10^{-14} in the analysis and forecast modes of the E1 experiment, respectively. Also, based on the other statistical results shown in Table 3, after implementing the DART/TIE-GCM, the overall RMSE of E1 is reduced by 81% and 77%, respectively. We also found the TND DA

Table 3
A Summary of the Statistical Measures Derived During the E1 Experiment Along the Orbit of CHAMP

Mode	RMSE (kg/m^3)	Bias (kg/m^3)	NASH	AAPD(%)	RE(%)
Original TIE-GCM	1.16×10^{-12}	-1.10×10^{-12}	−4.92	62.44	76.26
DART/TIE-GCM (Analysis)	2.20×10^{-13}	6.92×10^{-14}	0.78	8.61	14.42
DART/TIE-GCM (Forecast)	2.62×10^{-13}	5.77×10^{-14}	0.70	10.70	17.14

10.1029/2023SW003811

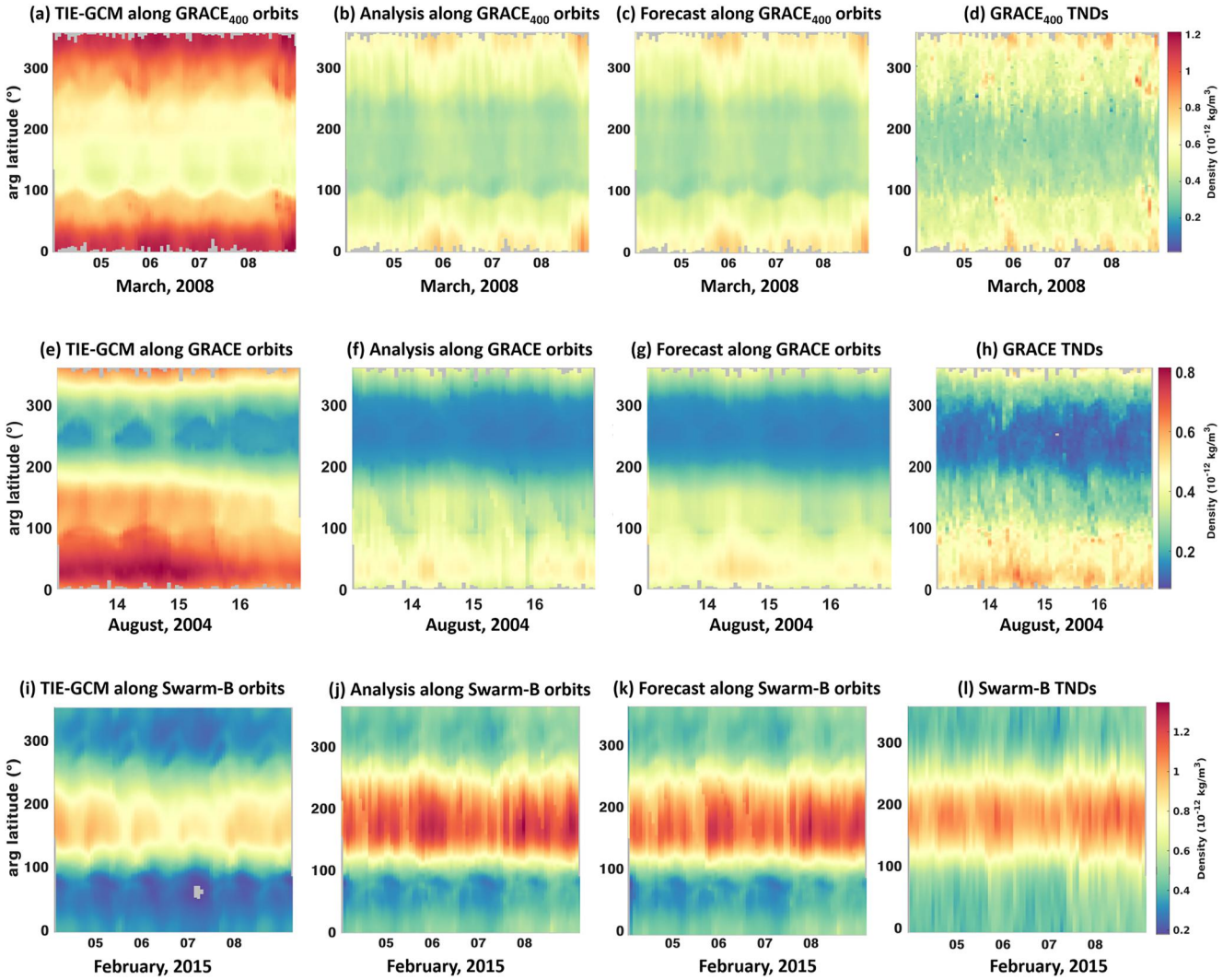

Figure 4. Validation with the TND data that are not used in the DA. TND estimates of TIE-GCM along the orbit of $GRACE_{400}$, GRACE and Swarm B (a, e, i); DART/TIE-GCM TND outputs in the analysis mode (b, f, j); DART/TIE-GCM TND outputs in the forecast mode (c, g, k); and the measured TNDs of $GRACE_{400}$, GRACE (485 km) and Swarm-B (521 km) in (d, h, l). The plots of a, b, c, and d refer to experiment E1 when the CHAMP-TNDs are used as assimilation observation, the plots of e, f, g, and h correspond to experiments E2, where DART/TIE-GCM is implemented using CHAMP TNDs as observation, while the plots of i, j, k, and l belong to the experiments E3, which DART/TIE-GCM is done based on the Swarm-C TNDs as observation.

to be very effective during the E2 and E3 experiments during high solar activity, where the results are presented in Appendix C and D.

4.3. Along-Track Validation of the DA TNDs During the Analysis and Forecast Phases

Here, the DART/TIE-GCM outputs are validated against measured TNDs that are not used during the DA procedure. For experiment E1 and E2 (done by CHAMP TNDs), and experiment E3 (done by Swarm-C), GRACE TNDs and Swarm-B TNDs are used for validation, respectively. It is worth mentioning that the altitude of GRACE orbits (i.e., 477 Km) during E1 is higher than the top level of TIE-GCM and DART/TIE-GCM (i.e., 460 Km). To avoid possible inconsistencies, we transformed GRACE TNDs to a common altitude of 400 km using Equation 4, and the inter-calibration of Equation 3 is applied. These estimates are called $GRACE_{400}$ in what follows. For experiments E2 and E3, GRACE and Swarm-B TNDs at altitude of 485 and 521 km are used, respectively.

Figure 4 shows maps of TNDs from TIE-GCM, and the DA's analysis and forecast steps, as well as those of $GRACE_{400}$, GRACE and Swarm-B as a function of time and the argument of latitude (the angle along the orbital

Table 4
A Summary of the Statistical Measures Derived During E1, E2 and E3 Experiments Along $GRACE_{400}$, GRACE (485 km) and Swarm-B (521 km) Orbits, Respectively

Time	Mode	RMSE (kg/m^3)	Bias (kg/m^3)	NASH	$Bias_{ratio}$ (%)	STD_{ratio} (%)
E1	Original TIE-GCM	3.88×10^{-13}	-3.67×10^{-13}	−11.85	0.55	15.27
	DART/TIE-GCM (Analysis)	8.85×10^{-14}	-5.74×10^{-14}	0.33	0.89	14.60
	DART/TIE-GCM (Forecast)	8.82×10^{-14}	-5.83×10^{-14}	0.33	0.88	14.49
E2	Original TIE-GCM	1.85×10^{-13}	-1.69×10^{-13}	−0.61	0.64	21.89
	DART/TIE-GCM (Analysis)	5.94×10^{-14}	1.40×10^{-14}	0.82	1.02	19.76
	DART/TIE-GCM (Forecast)	5.75×10^{-14}	7.09×10^{-15}	0.83	0.99	19.65
E3	Original TIE-GCM	1.87×10^{-13}	1.58×10^{-13}	0.48	1.37	19.27
	DART/TIE-GCM (Analysis)	7.41×10^{-14}	1.64×10^{-15}	0.91	1.00	16.99
	DART/TIE-GCM (Forecast)	8.17×10^{-14}	1.79×10^{-14}	0.90	1.02	17.91

Note. In E1 and E2 (E3) CHAMP-TNDs (Swarm-C (468 km)) are used as assimilated observations within the DART/TIE-GCM, and the results of original TIE-GCM, analysis and forecasting modes are evaluated.

path from the ascending node to the spacecraft's position in the direction of the spacecraft's motion). The plots on the top, middle, and bottom correspond to the E1, E2, and E3 experiments, respectively. Comparing Figure 4a with Figure 4d indicates that TIE-GCM overestimates the TNDs during E1 and E2, but it underestimates them during E3, compare Figure 4e with Figure 4h. These discrepancies are improved during both analysis and forecast modes, that is, Figures 4b or 4f and 4c or 4g are better fitted to (d or h) than (a or e). The numerical results of E1 indicate that the RMSE between TNDs from DART/TIE-GCM and $GRACE_{400}$ in the analysis and forecast modes are decreased by 77.1% and 77.3% compared to original TIE-GCM, respectively. Also, during E2, the RMSE of TNDs from TIE-GCM along the orbit of GRACE orbits is improved by 67.8% and 68.8% in the analysis and forecast modes after applying the DA. As well, during E3, the RMSE of TNDs from TIE-GCM along the orbit of Swarm-B orbits is reduced by 60.3% and 56.3% in the analysis and forecast modes after applying the DA. The detailed statistical assessments for the two experiments are provided in Table 4.

Further analysis is presented to explore the impact of the TND DA on TIE-GCM, where Figures 5a and 5d present the simulated TNDs of E1, E2, and E3 against the validation data in scatterplot. These plots support the investigation of Figure 4 by indicating the bias of TND simulations is considerably reduced after the DA (the reduction can be seen on the daily averages and for the day and night time separately). Considering the correlation coefficients, we found an increase from 0.45 for the original TIE-GCM to 0.77 and 0.79 for the analysis and forecast modes during E1, from 0.69 to 1.19 and 1.16 during E2, and from 1.3 to 0.99 and 1.04 during E3. The numerical details of this investigation can be found in Table 5. The results indicate that the original model simulates TNDs better during the nighttime better than the daytime (where solar activity is relatively higher). However, after implementing the TND DA of TIE-GCM, the ability of the model in forecasting TND in both periods is found to be similar.

4.4. Exploring the Impact of the TND DA on Spatial and Temporal Evolution of Thermosphere and Ionosphere Variables

To investigate how the TND DA affects model simulations, the Principal Component Analysis (PCA) (Forootan, 2014; Preisendorfer, 1988) method is applied to the differences between the original TIE-GCM and the forecast states of the DART/TIE-GCM. The input fields outputs of TNDs and electron density (altitude of 400 km) with 30-min intervals are considered here. The first two dominant modes of PCA are shown in Figures 6–8 that correspond to E1, E2, and E3, respectively. The spatial patterns from TND and Ne are known as Empirical Orthogonal Functions (EOFs that are anomaly maps in terms of density kg/m^3 and cm^{-3}) and their associated uncorrelated temporal patterns (Principal Components, or PCs that are unit-less) represent the orthogonal modes and are plotted along each other.

The first two dominant PCA modes during low solar activity (E1) correspond to 40.82% and 37.97% of the total variance of TND differences, and 38.34% and 29.81% of the Ne differences (see Figure 6). The temporal PCs are cyclic with diurnal frequency, which means that the TND DA likely modifies the diurnal time-scale the most

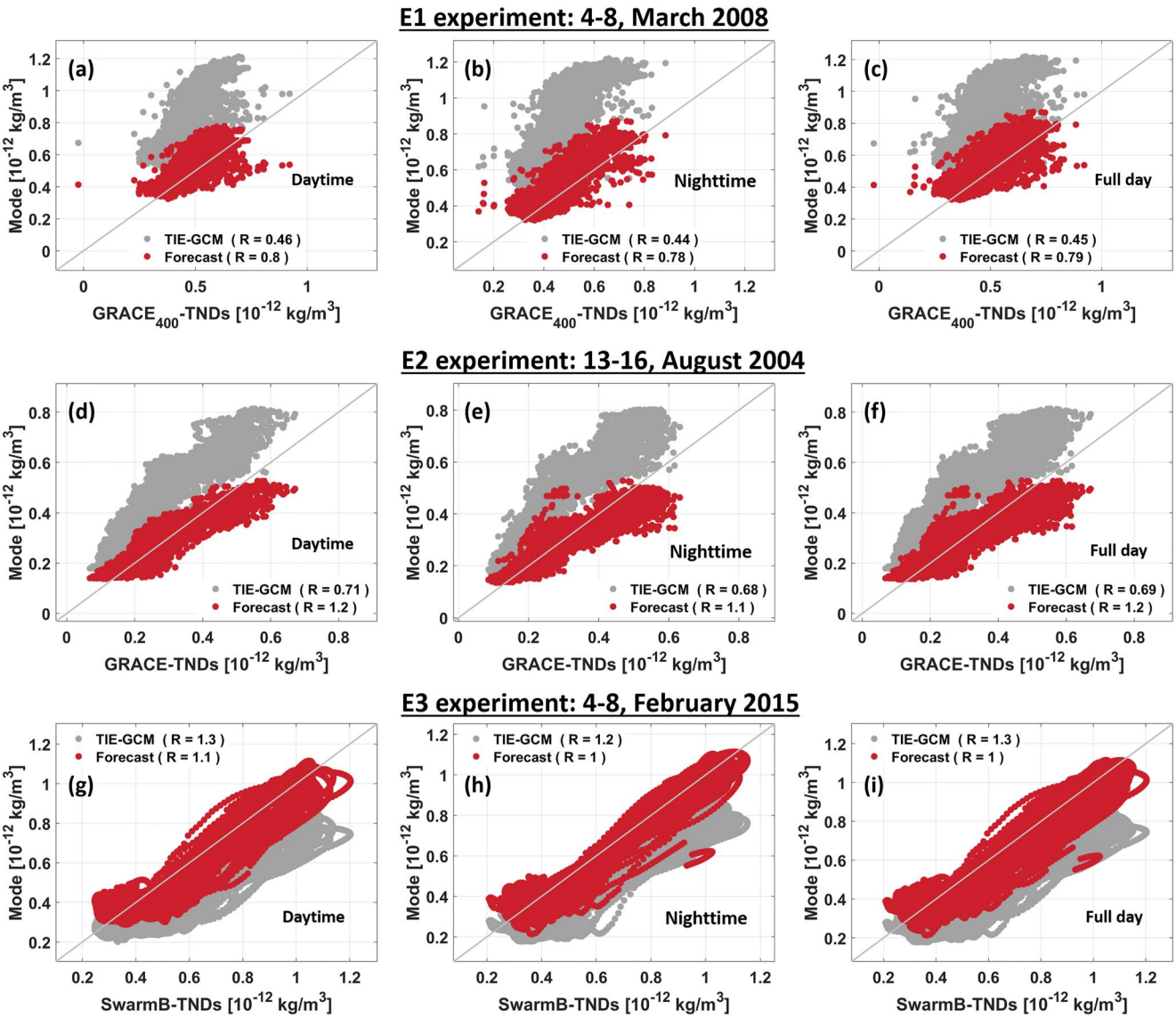

Figure 5. Scatter-plots of the TND validation during the experiment E1 (the three a to c plots on top), E2 (the d to e plots on middle), and E3 (the f to i plots on bottom). Separated day and time plots are shown in the first column for the daytime; and in the second column for the nighttime. The daytime orbit refers to 6–18 UT, and the nighttime corresponds to 18–24 and 0–6 UT. The third column represents the full-day $GRACE_{400}$, GRACE, and Swarm-B TNDs against TIE-GCM (gray dots) and the forecast mode of DART/TIE-GCM (red dots).

during low solar activity. The TND modes also indicate that the maximum differences after implementing the DA reach up to 25% of the original TIE-GCM. The similarity of EOF1 and EOF2 is related to the fact that PCA is a stationary statistical technique, and when the signals are cyclic they can be decomposed into (at least) two statistical modes. This is similar to the harmonics decomposition, where for a certain frequency both sine and cosine base functions are needed. In this study, EOF1 and PC1 correspond to the (semi) cyclic variability of TND and NE parameters with the daily period, whereas EOF2 and PC2 represent the out of phase variability. Therefore, There is a longitude shift in the pattern on EOFs. For the *Ne* differences (Figure 6), the maximum magnitude of first and second modes reach up to $1.85 \times 10^5\ cm^{-3}$ and $1.77 \times 10^5\ cm^{-3}$, respectively. Here, the magnitude is computed by multiplying the maximum value of EOFs with the maximum value of PC. The maximum changes of Ne after implementing the TND DA are discovered in low latitudes around ±30° latitude due to the dominant role played by the neutral wind dynamo in the low latitudes. This phenomenon refers to updating the electron density and neutral compositions along with the neutral winds and temperature in the assimilating procedure, which leads to the redistribution of atomic and molecular oxygen. This redistribution can have an influence on photoionization in

Table 5
A Summary of the Statistical Measures to Evaluate the TND DA (Using DART/TIE-GCM) Against the Validated TND Measurements of the $GRACE_{400}$, GRACE, and Swarm-B Missions During the E1, E2, and E3 Experiments

Time	Mode	RMSE (kg/m^3)	Bias (kg/m^3)	AAPD (%)	CC
Daytime (E1)	Original TIE-GCM	3.82×10^{-13}	-3.63×10^{-13}	83.23	0.46
	DART/TIE-GCM (Analysis)	8.5×10^{-14}	-5.5×10^{-14}	16.91	0.79
	DART/TIE-GCM (Forecast)	8.5×10^{-14}	-5.4×10^{-14}	17.06	0.80
Nighttime (E1)	Original TIE-GCM	3.94×10^{-13}	-3.71×10^{-13}	84.54	0.44
	DART/TIE-GCM (Analysis)	9.17×10^{-14}	-5.9×10^{-14}	17.65	0.76
	DART/TIE-GCM (Forecast)	9.12×10^{-14}	-6.17×10^{-14}	17.72	0.77
Daytime (E2)	Original TIE-GCM	1.85×10^{-13}	-1.68×10^{-13}	60.41	0.71
	DART/TIE-GCM (Analysis)	5.99×10^{-14}	1.29×10^{-14}	18.19	1.21
	DART/TIE-GCM (Forecast)	5.67×10^{-14}	0.70×10^{-14}	18.32	1.19
Nighttime (E2)	Original TIE-GCM	1.84×10^{-13}	-1.66×10^{-13}	60.19	0.68
	DART/TIE-GCM (Analysis)	5.88×10^{-14}	1.50×10^{-14}	15.17	1.17
	DART/TIE-GCM (Forecast)	5.83×10^{-14}	0.71×10^{-15}	15.79	1.13
Daytime (E3)	Original TIE-GCM	1.91×10^{-13}	1.59×10^{-13}	25.36	1.26
	DART/TIE-GCM (Analysis)	7.94×10^{-14}	4.45×10^{-15}	12.73	1.00
	DART/TIE-GCM (Forecast)	8.59×10^{-14}	2.06×10^{-14}	13.37	1.05
Nighttime (E3)	Original TIE-GCM	1.84×10^{-13}	1.57×10^{-13}	25.91	1.24
	DART/TIE-GCM (Analysis)	6.82×10^{-14}	-1.15×10^{-15}	11.62	0.99
	DART/TIE-GCM (Forecast)	7.73×10^{-14}	1.53×10^{-14}	12.30	1.03

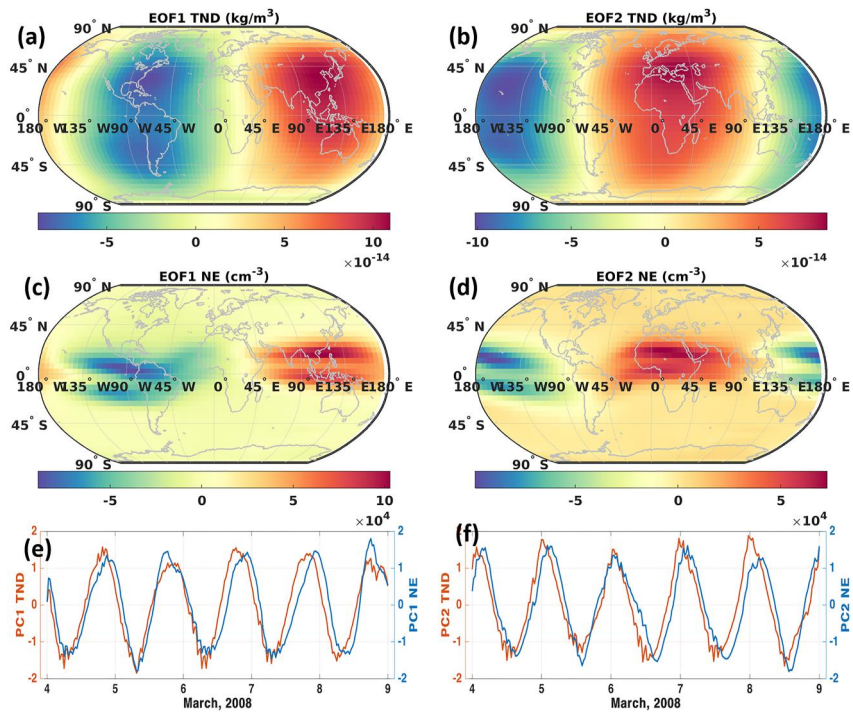

Figure 6. PCA of the TND and Ne differences derived between the outputs of TIE-GCM and the forecast mode of DART/TIE-GCM at 400 km altitude during E1 experiment. The left and right plots correspond to the first and the second modes of PCA, respectively. The anomaly maps (EOFs) (a and c) are shown in terms of kg/m^3 and cm^{-3}, respectively, which must be multiplied by the unit less time series (PCs) on the bottom of this figure (e and f). The first mode (left plots) represents 40.45% and 41.44% of the total variance of TND and Ne differences, respectively and the second mode of differences (right plots) indicates 38.01% and 32.92%.

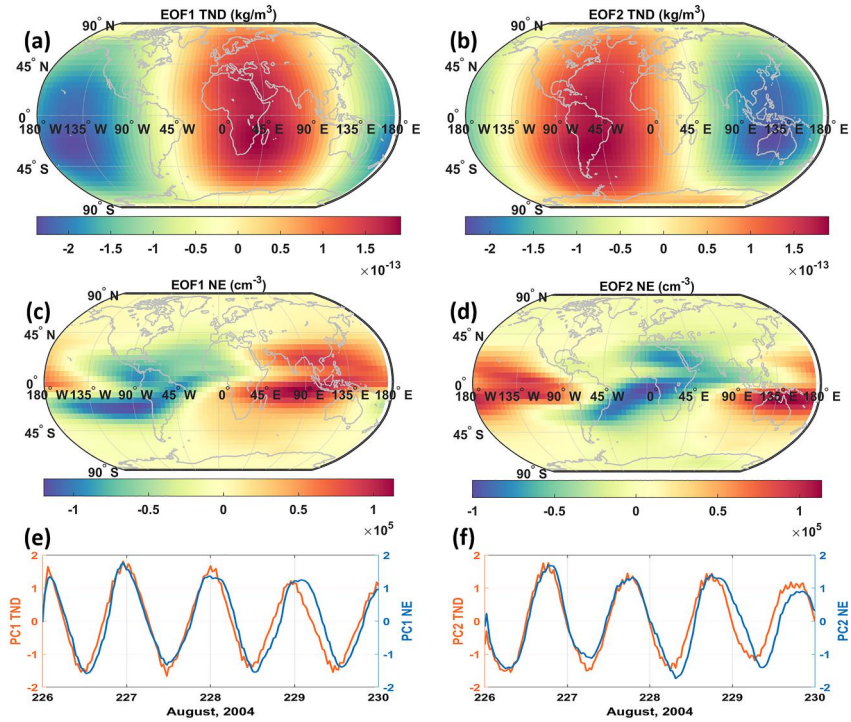

Figure 7. PCA of the TND and Ne differences derived between the outputs of TIE-GCM and the forecast mode of DART/TIE-GCM at 400 km altitude during E2 experiment. The left and right plots correspond to the first and the second modes, respectively. The anomaly maps (EOFs) (a and c) are presented in terms of kg/m^3 and cm^{-3}, which must be multiplied by the unit less time series (PCs) on the bottom of the figure (e and f) to derive the orthogonal modes. The first mode of differences (left plots) represents 34.87% and 36.20% of the total variance of TND and Ne differences, respectively. Following the same order of presentation, the second mode of differences (on the right) indicates 32.12% and 29.72% of the variance.

different regions. Since the neutral winds in the thermosphere drive ionospheric plasma circulation, they affect the density and distribution of charged particles in the ionosphere. These neutral winds are particularly powerful in the low latitudes due to the equatorial electrojet, a narrow band of strong eastward current in the ionosphere. As a result, any changes in the neutral density due to assimilation have a greater impact on the ionosphere electron density in the low latitudes than in other regions (Richmond et al., 1992; Jee et al., 2008; "Chapter 7—Ionosphere-thermosphere interaction", 2022). The PCs of Ne are also found to evolve after those of TND indicating that the diurnal modification of thermosphere parameters is well translated to the ionosphere parameters.

PCA is also applied on the TND and Ne changes after the TND DA during E2 and E3 with high solar activity. In the E2 experiment, the two dominant modes that are associated with 34.87 (36.20)% and 32.12 (29.72)% of the total variance of TND (Ne) differences are represented in Figure 7. Both TND modes contain patterns and fluctuations, ranging from -3.18×10^{-13} to 3.47×10^{-13} kg/m^3 and from -3.35×10^{-13} to 2.94×10^{-13} kg/m^3, respectively. The changes in TND had an impact on Ne variations (similar to E1), with the first two modes of Ne indicating a range of -1.80×10^5 to 2.01×10^5 cm^{-3} and -1.97×10^5 to 1.93×10^5 cm^{-3}, respectively.

Also, In the E3 experiment, the two dominant modes that correspond to 41.86 (25.98)% and 12.38 (23.98)% of the total variance of TND (Ne) differences are shown in Figure 8, respectively. Both TND modes contain diurnal fluctuations, where the magnitude of the differences are found to be in the range of -1.26×10^{-13}–-1.09×10^{-13} kg/m^3 and -1.05×10^{-12}–5.22×10^{-13} kg/m^3, respectively. Changes in the TNDs are translated to more pronounced Ne variations (compared to E1). The first two modes of Ne indicate that the impact of the TND DA is in the range of -2.01×10^5–2.26×10^5 cm^{-3} and -2.37×10^5–1.67×10^5 cm^{-3}, respectively. In the E3 experiment, the first mode of TND differences contains a trend (see Figure 8e, the red curve), which is driven by changes in the TND along assimilated mission (Swarm-C). The trend of the PC1 of Ne is found not to be as dominant as that of TND (compare the blue and red curves in Figure 8e), which is expected from the physics behind these two processes. The second mode of Ne is analogous to that of TND and similar to what we detected during E1 containing diurnal differences with the maximum changes around the EIA.

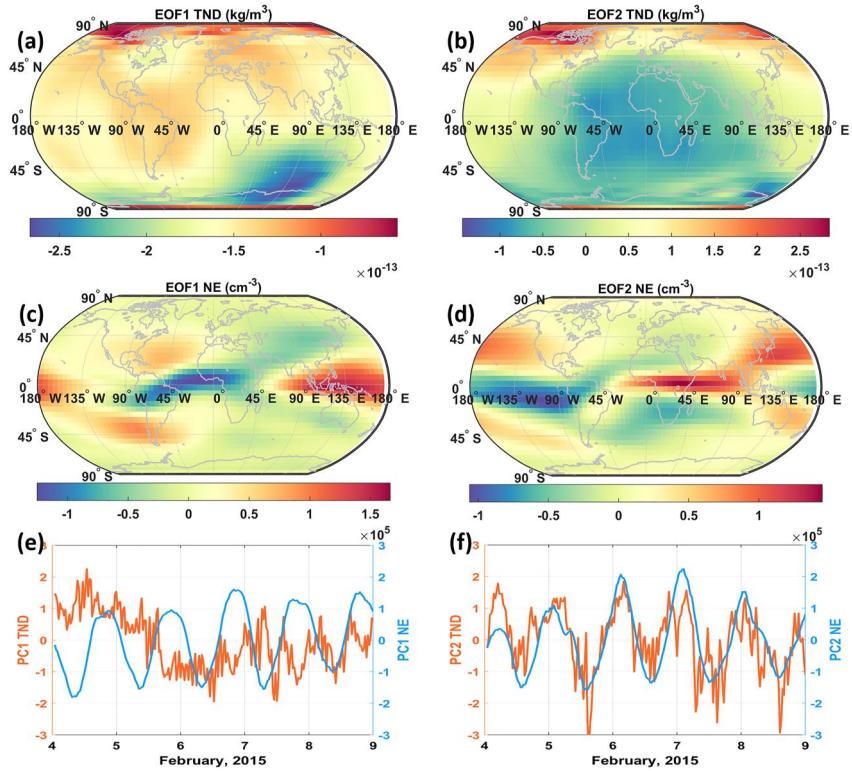

Figure 8. PCA of the TND and Ne differences derived between the outputs of TIE-GCM and the forecast mode of DART/TIE-GCM at 400 km altitude during E3 experiment. The left and right plots correspond to the first and the second modes, respectively. The anomaly maps (EOFs) (a and c) are presented in terms of kg/m^3 and cm^{-3}, which must be multiplied by the unit less time series (PCs) on the bottom of the figure (e and f) to derive the orthogonal modes. The first mode of differences (left plots) represents 41.86% and 25.98% of the total variance of TND and Ne differences, respectively. Following the same order of presentation, the second mode of differences (on the right) indicates 12.38% and 23.98% of the variance.

4.5. Validating the Forecast of Electron Density Using RO Data

The impact of thermosphere fields on the ionosphere parameters is evaluated using COSMIC data that were not used in the TND DA. For this evaluation, 1,853 and 1,250 Ne profiles during E1 and E3 experiments have been used covering the range of 80–700 km. It is noted that due to the unavailability of electron density profiles from COSMIC for August 2004, we were unable to include the E2 experiment in this section. Each Ne profile is interpolated through Bi-linear and cubic spline (De Boor, 1978) between 150 and 450 km with the height resolution of 10 km. Figures 9a–9c and 10a–10c show the vertical profiles of globally averaged electron density (COSMIC observations: green, the analysis mode of DART/TIE-GCM: blue, the forecast mode of DART/TIE-GCM: orange, and the original TIE-GCM: gray) during the full day, daytime and nighttime of the E1 and E3 experiments, respectively. Both figures indicate that the assimilation of TNDs has a considerable positive impact on forecasting Ne at altitudes above 250 km. The statistics indicate that the TND DA reduced the global RMSE of the Ne forecasts by 52.3% and 40.4% under low (E1) and high (E3) solar activity conditions, respectively, which indicate that the improvements during low solar activity (E1) is higher than the high solar activity (E3). Similar observations were drawn by Forootan et al. (2022) who replaced the TIE-GCM primary mass mixing ratio files with a better estimation of TNDs. The lack of impact below the altitude of 250 km could be attributed to the fact that the TND data is assimilated at relatively high altitudes. Besides, the large errors of COSMIC data at low altitudes (Lei et al., 2007; N. Pedatella et al., 2015; X. Yue et al., 2011) limits the certainty of the validation for low altitudes.

The results in Figures 9 and 10d, 10g show the daily scatter of Ne averaged in three latitude regions (low (20° S–20°N): gray dots, middle (20°–60°N/S): orange cross, high (60°–90°N/S): blue dots) between the Ne of

10.1029/2023SW003811

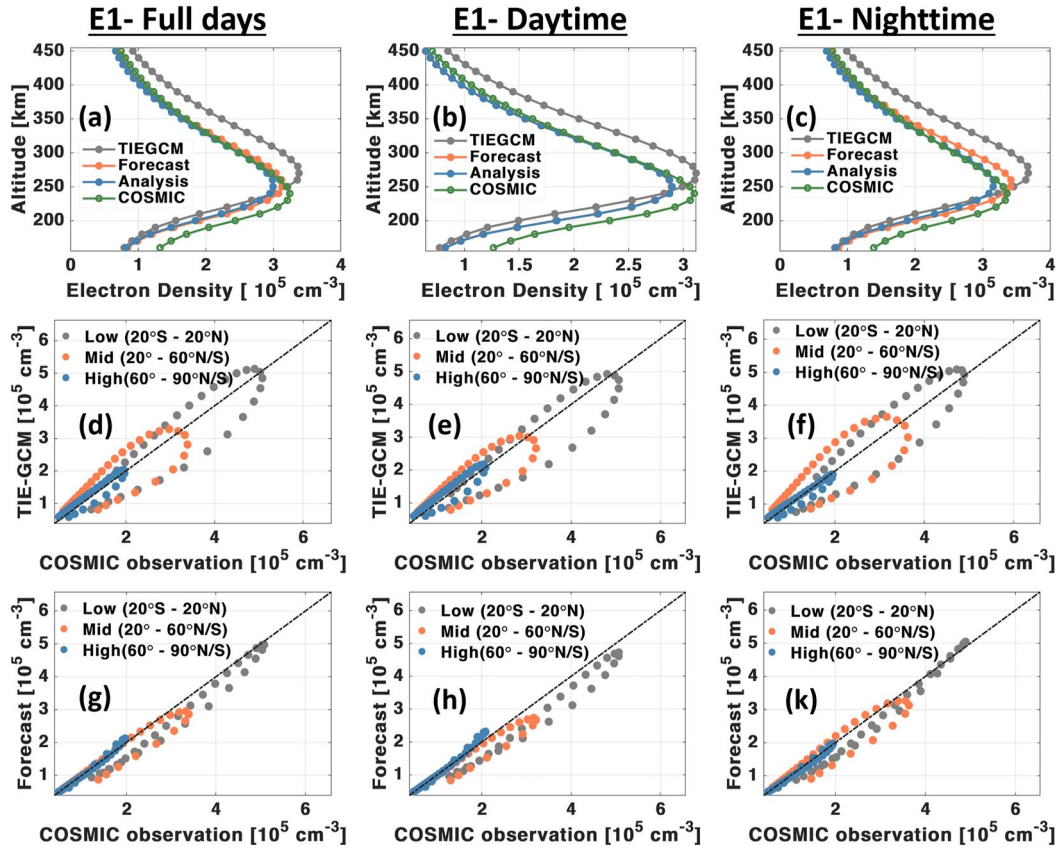

Figure 9. Independent evaluation of the TND DA with the Ne profiles of the COSMIC mission: (a, b, c) the global average Ne profiles of the full day, daytime, and nighttime during the E1 experiment; (d, e, f) multidimensional scatter plots of TIE-GCM Ne against COSMIC during full day, daytime and nighttime of E1; and (g, h, k) multidimensional scatter plots of the DART/TIE-GCM in the forecast mode against COSMIC during the full day, daytime and nighttime of E1. The results are separated for the three latitude regions of low, mid, and high.

COSMIC and TIE-GCM, as well as between the Ne of COSMIC and the forecast state of DART/TIE-GCM during the E1 and E3 experiments, respectively. The corresponding daytime averages are shown in Figures 9 and 10e, 10h and those of nighttime are shown in Figures 9 and 10f, 10k. After the TND DA, numerical assessments demonstrate that the global relative error of Ne forecast in the daytime improved from 1.32 (1.22) to 0.69 (0.60) and those of nighttime decreased from 1.62 (1.04) to 0.74 (0.79) during E1 (E3). Other statistical evaluations are provided in Table 6. In terms of the latitude regions, the statistical measurements represent that relative error and correlation coefficient are improved from 1.07 and 0.89 to 0.71 and 0.99 in the low, from 1.64 and 0.80 to 0.97 and 0.95 in the middle and from 0.69 and 0.95 to 0.31 and 0.99 in the high latitude regions during E1. These results indicate that bigger improvements in the mid compared to the low and high latitude regions.

5. Conclusions

A logical step to make the best use of available measurements and models can be realized by integrating them through Data Assimilation (DA) frameworks. In this study, we presented the impact of DA based on the Ensemble Kalman Filter (EnKF) on updating the physics-based model states. The Data Assimilation Research Testbed (DART) community software is used to merge the physics-based TIE-GCM model with TNDs that are sampled along the CHAMP and Swarm-C satellite orbits. The TND DA results are called DART/TIE-GCM. This implementation was performed during three periods with low (E1, $F_{10.7}$ = 70 SFU) and high (E2 and E3, $F_{10.7}$ = 140 SFU) solar activity. We also tested the impact of localization and real LEO-derived estimates on the

10.1029/2023SW003811

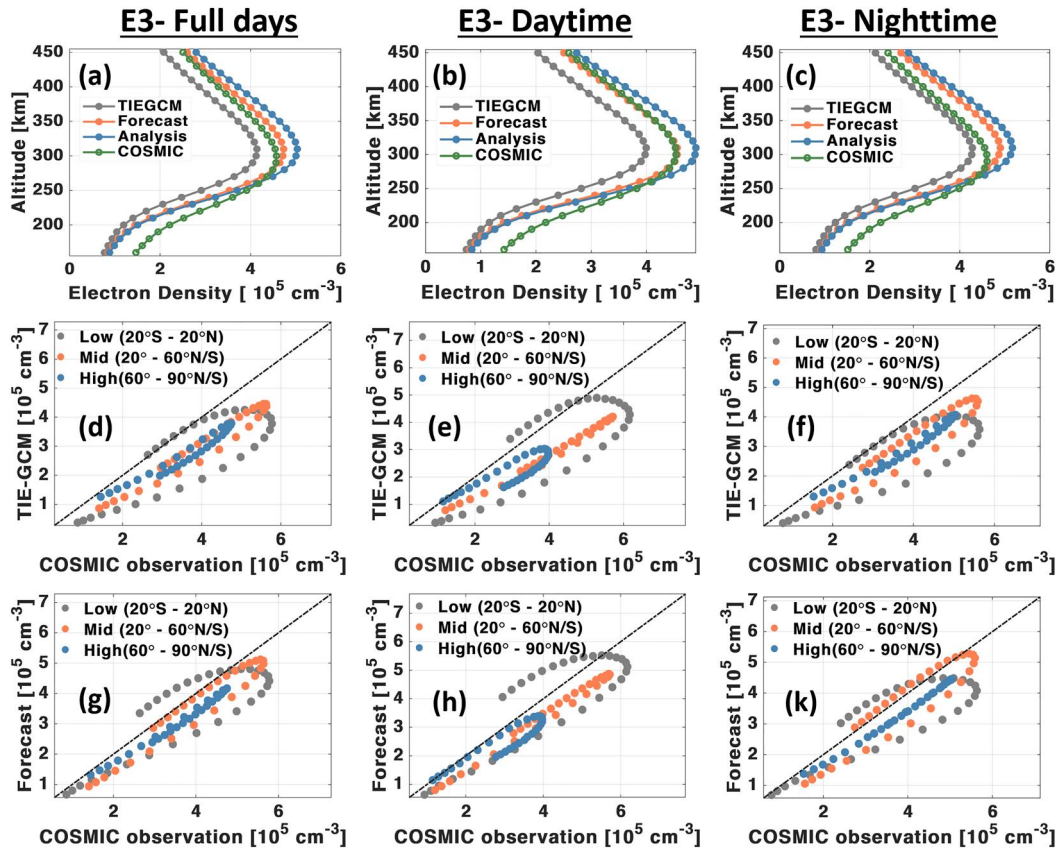

Figure 10. Independent evaluation of the TND DA with the Ne profiles of the COSMIC mission: (a, b, c) the global average Ne profiles of the full day, daytime, and nighttime during the E3 experiment; (d, e, f) multidimensional scatter plots of TIE-GCM Ne against COSMIC during full day, daytime and nighttime of E3; and (g, h, k) multidimensional scatter plots of the DART/TIE-GCM in the forecast mode against COSMIC during the full day, daytime and nighttime of E3. The results are separated for the three latitude regions of low, mid, and high.

Table 6

A Summary of the Statistical Measures to Evaluate the TND DA (Using DART/TIE-GCM) Against the Ne Measurements of the COSMIC Mission During the E1 and E3 Experiments

Time	Mode	RMSE (10^5 cm^{-3})	RE (%)	AAPD (%)	NASH	CC
Full-time (E1)	Original TIE-GCM	0.52	1.44	26.12	0.57	0.81
	DART/TIE-GCM (Forecast)	0.25	0.68	9.10	0.90	0.96
Day-time (E1)	Original TIE-GCM	0.45	1.32	23.35	0.65	0.83
	DART/TIE-GCM (Forecast)	0.24	0.69	9.90	0.90	0.97
Night-time (E1)	Original TIE-GCM	0.61	1.62	29.66	0.45	0.78
	DART/TIE-GCM (Forecast)	0.28	0.74	9.99	0.88	0.95
Full-time (E3)	Original TIE-GCM	0.69	1.12	22.04	0.46	0.97
	DART/TIE-GCM (Forecast)	0.40	0.65	12.65	0.81	0.97
Day-time (E3)	Original TIE-GCM	0.75	1.22	24.63	0.36	0.98
	DART/TIE-GCM (Forecast)	0.37	0.60	10.80	0.84	0.99
Night-time (E3)	Original TIE-GCM	0.64	1.04	19.11	0.54	0.94
	DART/TIE-GCM (Forecast)	0.48	0.79	16.10	0.73	0.95

analysis and forecasts of the DART/TIE-GCM system. The results are then validated in terms of TNDs along the GRACE and Swarm-B, which were not used in the DA procedure. To understand the impact of updating TNDs on forecasting ionospheric variables, the output of DART/TIE-GCM is evaluated with electron density (Ne) profiles of the COSMIC mission. Therefore, by this evaluation, one may consider that the DA of thermosphere-related variables is validated against ionosphere-related measurements.

The main findings of this study are summarized as:

- Updating the state vectors in the global EnKF-based DA highly depends on the localization of the covariance matrix, which is controlled by the so called cut-off radius in the Schur product implementation (Gaspari & Cohn, 1999) of DART. Our investigations indicate that the bias between original TIE-GCM and TND measurements is reduced from 3.61×10^{-13} to 1.12×10^{-13}, 0.71×10^{-13}, and 0.58×10^{-13} after implementing DA with cutoff values of 0.2, 1 and 3, respectively. The cutoff value of three for the horizontal localization is found to provide better statistical measures in the forecast mode. In all investigations of this study, vertical localization was not introduced to allow the TND DA to extend the updates to the entire model levels. This is particularly important for the forecast of ionosphere variables that exhibit considerable vertical coupling (Ridley et al., 2006).
- After implementing the TND DA, the density and temperature of the coupled model change, which has an impact on the vertical distances between the consecutive pressure layers. To achieve a correct conversion, we suggest adding the geopotential height to the state vector and the impact of the estimated temperature and composition have been used to update the geopotential and geometric heights. A formulation is provided to update the geometric heights after performing the TND DA. The numerical results in the analysis and forecast modes (Section 4.2) show that the conversion in the height is well performed and the discrepancies are not originated from the conversion.
- The TND validations along the orbits of GRACE and Swarm-B (E1, March 4*th*–8*th*, 2008 and E2, August 13*th*–16*th*, 2004 and E3, February 4*th*–8*th*, 2015) indicate that the differences between the original TIE-GCM and DART/TIE-GCM outputs are considerably reduced. The RMSE results indicate 79% reduction in the forecasting step during E1, 68% during E2, and 51% during E3. This result indicates that the impact of the assimilation on TND was bigger during low solar activity compared to the high solar activity period.
- The spatial and temporal modes of differences between the TNDs and Ne derived from the original TIE-GCM and DART/TIE-GCM in the forecast mode are explored using the principal component analysis (PCA) technique. The first two dominant modes of anomalies indicate that the TND DA affects the diurnal time-scale of thermosphere and ionosphere simulations during low solar activity, which can be well transferred to the forecast of Ne. During the high solar activity, the variation of TND is translated in the first mode of TND differences, see Figure 8. The second mode on TNDs was dominated by diurnal fluctuations as expected. These modifications are found to be well transformed to the forecasts of Ne with the maximum effect to be reached around Equatorial Ionization Anomaly (EIA, around ±30° latitude, see Figures 6–8).
- The results demonstrated in Figures 9 and 10 indicate that assimilating LEO-derived TNDs in TIE-GCM impacts the analysis and forecast of the electron density during both low and high solar activity periods. Our experiments show that the DART/TIE-GCM with assimilating TNDs is able to decrease the errors of Ne by 52.3% and 40.4% in the forecast mode compared to the Ne measured by RO during E1 and E3. Therefore, the impact on Ne is found to be larger during low solar activity compared to high solar activity. Analogous to the TND behavior, the original TIE-GCM overestimates (underestimates) Ne during the period with low (high) solar activity. The TND DA can mitigate this mis-modeling from 52,613 (69,603) cm^{-3} to 25,078 (40,636) cm^{-3} in terms of RMSE during E1 (E3).

This study mainly focused on the assimilation of space-based TNDs into TIE-GCM during periods with low and high solar activity. This work can be extended by considering multi-sensor data such as the radio occultation-derived electron density profiles, GNSS-derived total electron content, as well as thermospheric neutral winds and temperature. Also, the advantage of this DA implementation for the near-real time orbit prediction and point positioning applications can be further explored. To improve the forecasting ability, it will be helpful to conduct further research on the calibration of external forcing (Forootan et al., 2020, 2022; Kosary et al., 2022) using multi-sensor measurements.

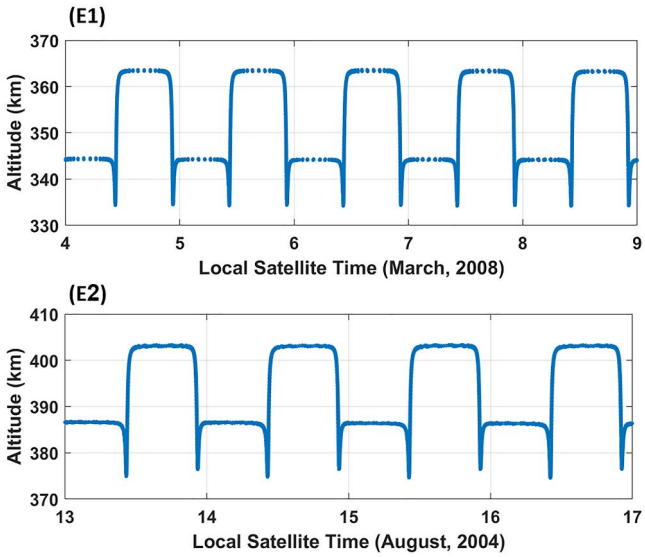

Figure A1. Variation of altitude against local satellite time along CHAMP orbits during the E1 (top) and E2 (bottom) experiments.

Appendix A: Data Set

A1. CHAMP

The CHAMP satellite was launched in June 2000 into an 87° inclination orbit, at an initial altitude of 454 km with an orbital period of 93.55 min. Because the orbital height of these satellites was low (less than 550 km), accelerometer sensors were installed to assess non-gravitational forces operating on their surface. The main source of non-gravitational acceleration at low altitudes is atmospheric drag caused by the satellite's movement through the thermosphere. SO, TNDs along CHAMP orbits can be estimated through raw accelerometer observation. In this study, CHAMP TNDs are derived from TU Delft (Siemes et al., 2023) at a 30-s sampling rate and The time-series of altitude against the local time of the satellites during E1 and E2 experiments of this study are displayed in Figure A1.

A2. GRACE

The Gravity Recovery and Climate Experiment (GRACE, 2002–2017) (Tapley et al., 2004) and its follow-on mission (GRACE-FO, launched in 2018) (Flechtner et al., 2014), were designed to provide information about the Earth's gravity field. The two satellites, GRACE-1 and GRACE-2, were initially in a circular polar co-planar orbit at an altitude of 500 km, which eventually decayed to 300 km, and were at an inclination of 89° with 90 min orbital period. Similar to CHAMP, the accelerometer on the GRACE and GRACE-FO provide observations that are utilized to determine TND along satellite orbits (Doornbos, 2012; Sutton, 2011; Sutton et al., 2007). In this study, the GRACE1-TNDs are derived from TU Delft (Siemes et al., 2023) at a 30-s sampling rate. The variation of altitude against the local time of the satellites during E1 and E2 experiments of this study are shown in Figure A2.

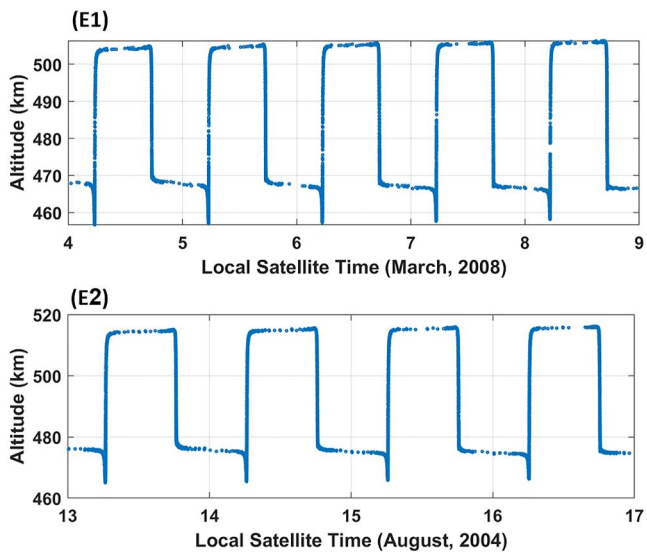

Figure A2. Variation of altitude against local satellite time along GRACE orbits during the E1 (top) and E2 (bottom) experiments.

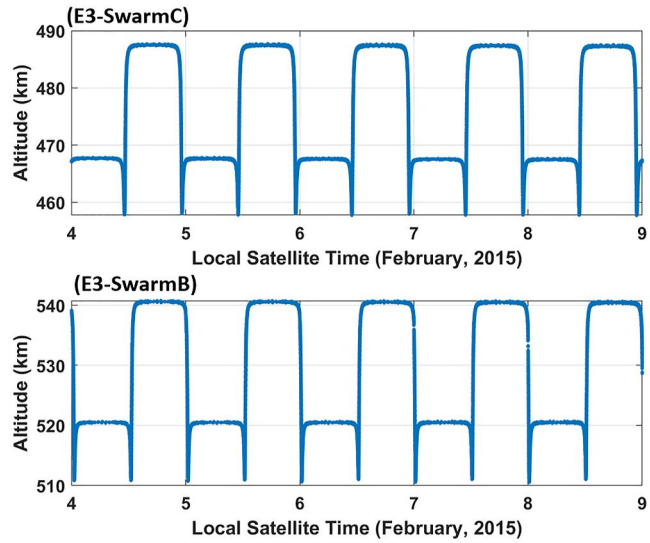

Figure A3. Variation of altitude against local satellite time along Swarm-C (top) and Swarm-B (bottom) orbits during the E3 experiment.

A3. Swarm

The three Swarm satellites were launched on 22 November 2013, into near-polar orbits. Swarm A and C are the lower pair of satellites, flying side by side (1.4° separation in longitude at the equator) at an altitude of 462 km (initial altitude), an inclination angle of 87.35° and an orbital period of 94 min. Each Swarm satellite carries an accelerometer and GPS receiver. These measurements can be used for determining non-gravitational forces such as drag and radiation pressure acting on the spacecraft. In this study, the high-quality TNDs from Swarm GPS observations are used and their estimation procedure is summarized in two steps in the following (Van Den IJssel et al., 2020). At first, the non-gravitational accelerations are estimated in a GPS-based precise orbit determination (POD) procedure. In the second step, the direct approach (Doornbos et al., 2010) is used to convert the accelerations into thermospheric densities. In this study, Swarm-TNDs from GPS data is downloaded from http://thermosphere.tudelft.nl/ at a 30-s sampling rate. The changes in altitude against the local time of the satellites during the E3 experiment of this study are represented in Figure A3.

Appendix B: Evaluation Measures

To numerically evaluate the performance of the data assimilation procedure in analysis and forecast steps compared to the observation, the following metrics are applied:

- "Bias" is defined as:

$$\text{Bias} = \frac{1}{n}\sum_{i=1}^{n}(\text{Obs}_i - \text{Model}_i), \tag{B1}$$

where Obs and Model denote observation and model estimates, receptively, and n is the number of observations. The positive (negative) values of the bias demonstrate that the model underestimates (overestimates) compared to the observations.

- The expression of bias in percentage is computed based on the "Relative Error (RE)" as:

$$\text{RE} = 100 \times \sum_{i=1}^{n}\left(\frac{|\text{Obs}_i - \text{Model}_i|}{\text{Obs}_i}\right), \tag{B2}$$

where |.| represents an operator that returns the absolute values.

- Bias of density ratio is defined as:

$$\text{Bias}_{\text{ratio}} = \frac{1}{n}\sum_{i=1}^{n}(\text{Exp}(\text{Ln}(\text{Obs}_i/\text{Model}_i))), \tag{B3}$$

When the value of $\text{Bias}_{\text{ratio}}$ is less than 1 (larger than 1), the metric indicates that the model overestimate (underestimate) the feature.

- "Root Mean Squares of Error (RMSE)" is determined to assess how model estimates match with observations as:

$$\text{RMSE} = \sqrt{\frac{\sum_{i=1}^{n}(\text{Obs}_i - \text{Model}_i)^2}{n}} \tag{B4}$$

The square term inside the RMSE equation highlights both positive and negative differences between the quantities.

- "Improvement" is defined as percentage in the computed RMSEs after implementing DDA as:

$$\text{Improvement} = 100 \times \frac{\text{RMSE}_1 - \text{RMSE}_2}{\text{RMSE}_1}, \tag{B5}$$

where RMSE_1 is computed between the original TIE-GCM and observations, and RMSE_2 is determined between DART/TIE-GCM outputs and observations.

- "Average of Absolute Percentage Deviation (AAPD)" is expressed as the percentage of absolute difference between observation and model as:

$$\text{AAPD} = 100 \times \frac{\sum_{i=1}^{n}\left(\left|\frac{\text{Obs}_i - \text{Model}_i}{\text{Obs}_i}\right|\right)}{n}, \tag{B6}$$

Minimum (maximum) values of AAPD correspond to the average best (worst) performance of a model in estimating VTECs.

- "Nash" Nash-Sutcliffe model Efficiency Coefficient is represented the fraction of the variance in the data that is predicted by the model as:

$$\text{Nash} = 1 - \frac{\sum_{i=1}^{n}(\text{Obs}_i - \text{Model}_i)^2}{\sum_{i=1}^{n}\left(\text{Obs}_i - \overline{\text{Obs}}\right)^2}, \tag{B7}$$

where $\overline{\text{Obs}}$ is defined as the mean of observations. In contrast to AAPD, the minimum (maximum) values of Nash correspond to the average worst (best) performance of model in simulating VTECs.

- "$\text{STD}_{\text{ratio}}$" presents the ability of the model to simulate observed TND change, as well as geophysical noise and instrumental noise in the observations (Bruinsma et al., 2018) and it is determined as:

$$\text{STD}_{\text{ratio}} = 100 \times (\text{Exp}(\text{STD}(\text{Ln}(\text{Obs}/\text{Model}))) - 1), \tag{B8}$$

where StD is Standard Deviation of the density ratio.

- "Correlation Coefficients (CCs)" are used as a unit-less measure to represent the overall fit between model estimations and observations:

$$\mathrm{CC} = \frac{\sum_{i=1}^{n}\left(\mathrm{Model}_i - \overline{\mathrm{Model}}\right)\left(\mathrm{Obs}_i - \overline{\mathrm{Obs}}\right)}{\sqrt{\sum_{i=1}^{n}\left(\mathrm{Model}_i - \overline{\mathrm{Model}}\right)^2 \sum\left(\mathrm{Obs}_i - \overline{\mathrm{Obs}}\right)^2}}. \tag{B9}$$

The range of CCs is from −1 to +1, where −1 indicates the perfect negative correlation, +1 corresponds to the 100% fit, and zero indicates no correlations.

Appendix C: Impact of the TND DA on Reducing Biases During the E2 Experiment With High Solar Activity

The effects of the TND DA along CHAMP during the E2 experiment with high solar activity are shown in Figure C1. These plots indicate the ability of DART/TIE-GCM during high solar activity period and the bias values are decreased from 3.96×10^{-13} to 7.48×10^{-14} and 1.25×10^{-13} in the analysis and forecast modes, respectively. Also, in the data assimilation procedure, the RMSE values are improved by 64% and 49% in the analysis and forecast modes, respectively. The statistical measures such as RMSE, Bias, Nash as well as RE are reported in Table C1.

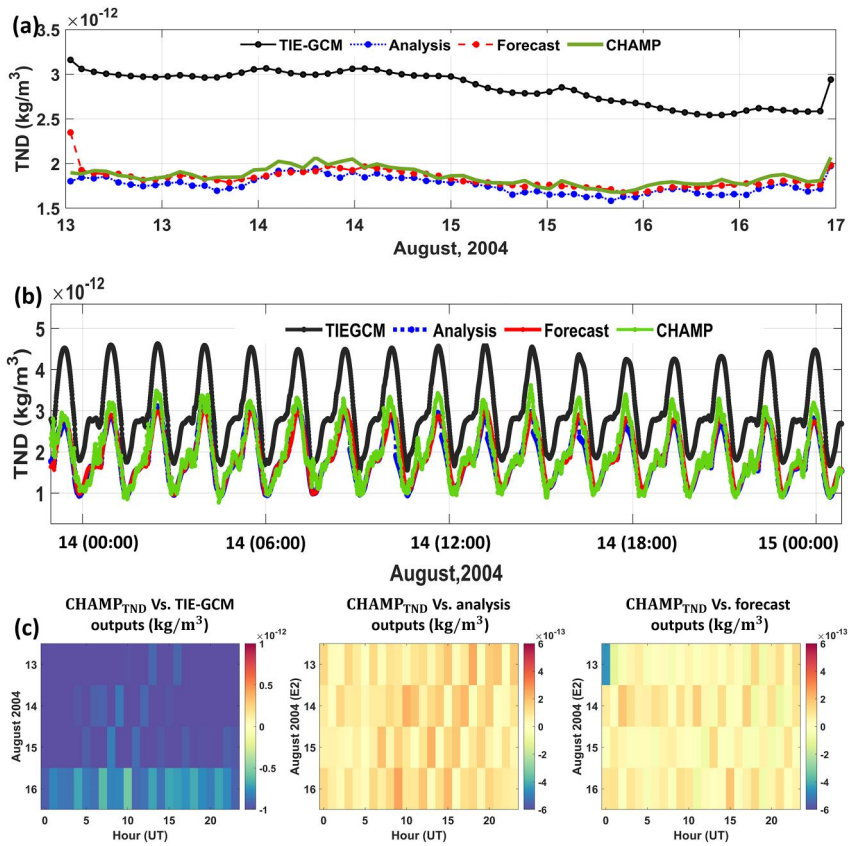

Figure C1. Comparisons of the DA TND with CHAMP measurements during high solar activity: (a) orbit-averaged TNDs from TIE-GCM, DART/TIE-GCM outputs in the analysis and forecast modes, as well as measured TNDs along the orbit of CHAMP during the E2 experiment (August 13^{th}–16^{th}, 2004); (b) Time-series of TNDs during 24 hr in 14 August 2004; and (c) a summary of biases (from Equation B1) between the measured TNDs and those of TIE-GCM and DART/TIE-GCM. Here, the DART/TIE-GCM is processed using CHAMP TNDs as assimilation observations.

Table C1
A Summary of Statistical Measures Derived During the E2 Experiment Along the Orbit of CHAMP

Mode	RMSE (kg/m^3)	Bias (kg/m^3)	NASH	AAPD(%)	RE(%)
Original TIE-GCM	1.05×10^{-12}	-1.01×10^{-12}	−1.57	58.74	60.98
DART/TIE-GCM (Analysis)	2.09×10^{-13}	9.41×10^{-14}	0.89	8.02	12.16
DART/TIE-GCM (Forecast)	2.23×10^{-13}	2.75×10^{-14}	0.88	9.71	12.99

Note. Here the CHAMP TNDs are used as assimilation observations within the DART/TIE-GCM implementation, and the results of the original TIE-GCM, the DA models in the analysis, and forecast modes are evaluated.

Appendix D: Impact of the TND DA on Reducing Biases During the E3 Experiment With High Solar Activity

Effects of the TND DA along Swarm-C during the E3 experiment with high solar activity are presented in Figure D1. These plots show that the DART/TIE-GCM is effective in high solar activity and the bias values are reduced from 3.96×10^{-13} to 7.48×10^{-14}, and 1.25×10^{-13} in the analysis and forecast modes, respectively. Our experiments indicate that DART/TIE-GCM is able to decrease the RMSE by 64% and 49% in the analysis and forecast modes, respectively. Different statistical measures such as RMSE, Bias, Nash as well as RE are reported in Table D1.

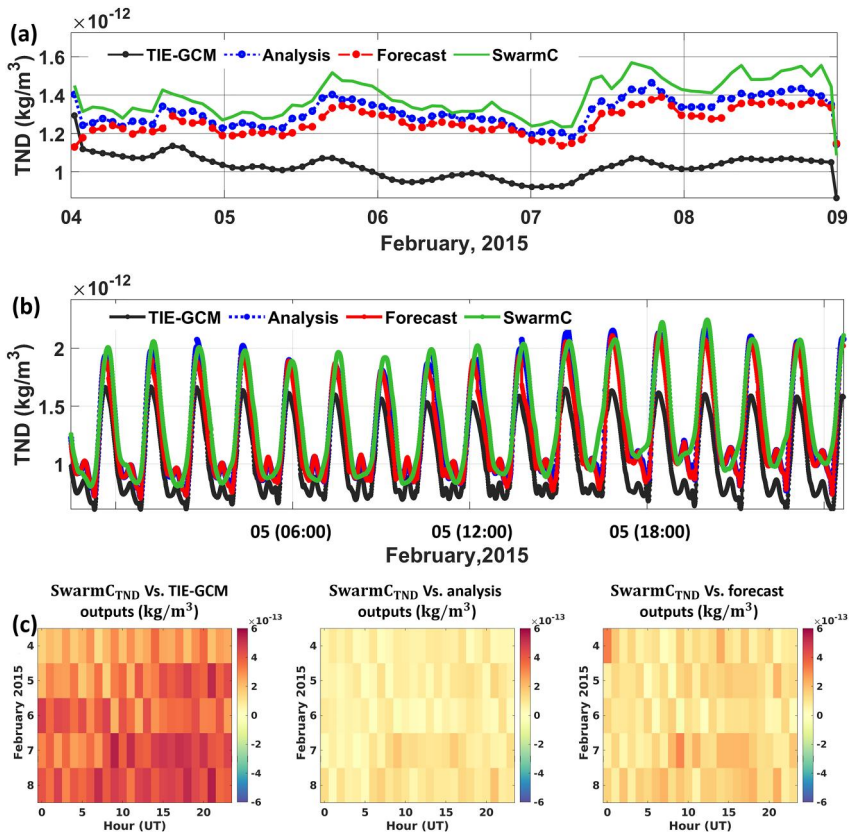

Figure D1. Comparisons of the DA TND with Swarm-C measurements during high solar activity: (a) orbit-averaged TNDs from TIE-GCM, DART/TIE-GCM outputs in the analysis and forecast modes, as well as measured TNDs along the orbit of Swarm-C during the E2 experiment (February 4^{th}–8^{th}, 2015); (b) Time-series of TNDs during 24 hr in 5 February 2015; and (c) a summary of biases (from Equation B1) between the measured TNDs and those of TIE-GCM and DART/TIE-GCM. Here, the DART/TIE-GCM is processed using Swarm-C TNDs as assimilation observations.

Table D1
A Summary of Statistical Measures Derived During the E3 Experiment Along the Orbit of Swarm-C

Mode	RMSE (kg/m^3)	Bias (kg/m^3)	NASH	AAPD (%)	RE (%)
Original TIE-GCM	3.96×10^{-13}	3.58×10^{-13}	0.05	25.74	34.29
DART/TIE-GCM (Analysis)	1.41×10^{-13}	7.48×10^{-14}	0.88	8.62	12.21
DART/TIE-GCM (Forecast)	2.01×10^{-13}	1.25×10^{-13}	0.75	11.68	17.37

Note. Here the Swarm-C TNDs are used as assimilation observations within the DART/TIE-GCM implementation, and the results of the original TIE-GCM, the DA models in the analysis, and forecast modes are evaluated.

Figures 3, C1, and D1 and numerical results in Tables 3, C1, and D1 during periods with low and high solar activity highlighted the ability of data assimilation procedure in estimating the TNDs with high accuracy in analysis and forecasting model along assimilated observations orbits. Also, These results show the magnitude of improvements might be lower during days with a high solar activity index.

Appendix E: Exploring the Third Mode of Applying PCA Technique on the Neutral Density and Electron Density During E3

The third modes of PCA during high solar activity (E3) correspond to 9.63% and 13.16% of the total variance of TND and Ne differences, respectively (see Figure E1).

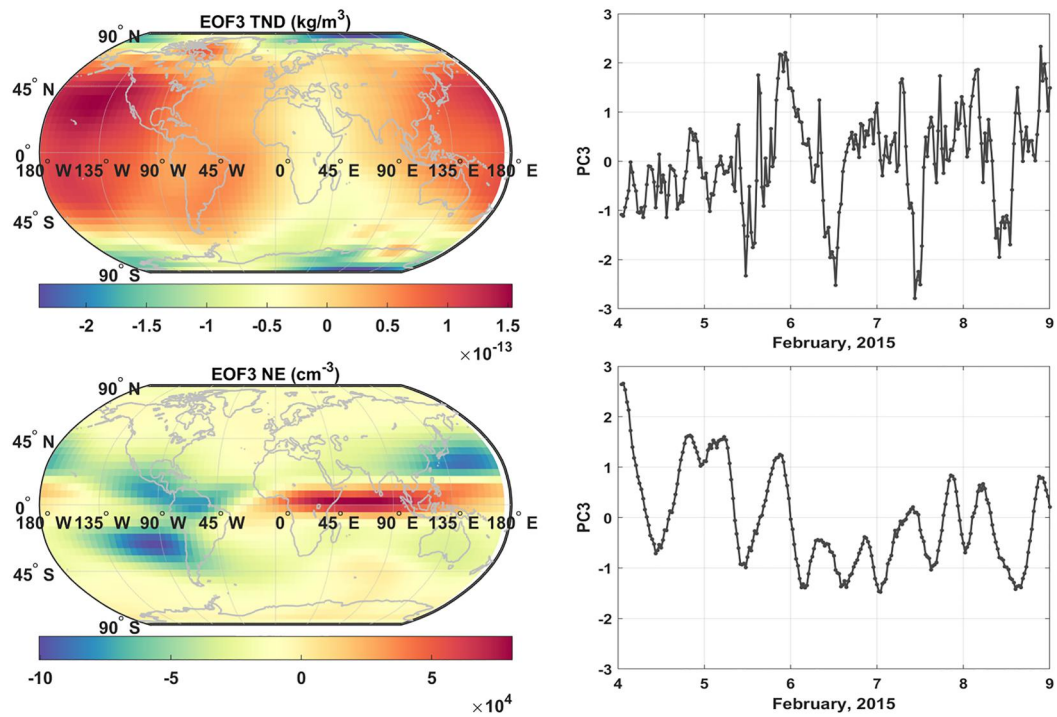

Figure E1. PCA of the TND and Ne differences derived between the outputs of TIE-GCM and the forecast mode of DART/TIE-GCM at 400 km altitude during E3 experiment. The left corresponds to the third mode of PCA. The anomaly maps (EOFs) are shown in terms of kg/m^3 and cm^{-3}, which must be multiplied by the unit less time series (PCs) on the right side of this figure.

Data Availability Statement

The authors are very grateful to the providers for their data that were freely available to this study. The UCAR/DART provided the data assimilation tools used in this work (J. L. Anderson et al., 2004). The source code for the simulation models used in this study, TIE-GCM, is freely available from https://www.hao.ucar.edu/modeling/tgcm/tie.php. The thermosphere neutral density data along the orbit of CHAMP, GRACE and Swarm are available from the Delft Technical University's website (Siemes et al., 2023; Van Den IJssel et al., 2020). The solar activity index $F_{10.7}$ and the geomagnetic activity index *Kp* data are available from the following links: $F_{10.7}$: https://www.spaceweather.gc.ca/forecast-prevision/solar-solaire/solarflux/sx-en.php and *Kp*: https://doi.org/10.5880/Kp.0001. The COSMIC data are available from http://www.cosmic.ucar.edu. This paper's main data assimilation results have been published on the Zenodo website (Kosary et al., 2024).

Acknowledgments
The authors thank Delft University for providing access to neutral density data along CHAMP, GRACE, and Swarm orbits, which were obtained from Delft ftp (ftp://thermosphere.tudelft.nl/). The Constellation Observing System for Meteorology, Ionosphere, and Climate (COSMIC) data were downloaded from the COSMIC Data Analysis and Archival Center (https://www.cosmic.ucar.edu/what-we-do/cosmic-1/data/). The DART software was obtained from the NCAR (http://www.image.ucar.edu/DAReS/DART). The Thermosphere Ionosphere Electrodynamics General Circulation Model software was obtained from High Altitude Observatory, NCAR (http://www.hao.ucar.edu/modeling/tgcm/tie.php). The authors are grateful for the comments provided by anonymous reviewers, which helped us to improve the quality of this study.

References

Aa, E., Liu, S., Huang, W., Shi, L., Gong, J., Chen, Y., et al. (2016). Regional 3-d ionospheric electron density specification on the basis of data assimilation of ground-based GNSS and radio occultation data. *Space Weather*, *14*(6), 433–448. https://doi.org/10.1002/2016SW001363

Albertella, A., Migliaccio, F., & Sansó, F. (2002). GOCE: The Earth gravity field by space gradiometry. In *Modern celestial mechanics: From theory to applications* (pp. 1–15). Springer. https://doi.org/10.1007/978-94-017-2304-6_1

Anderson, J. (2001). An ensemble adjustment Kalman filter for data assimilation. *Monthly Weather Review*, *129*(12), 2884–2903. https://doi.org/10.1175/1520-0493(2001)129⟨2884:AEAKFF⟩2.0.CO;2

Anderson, J., Hoar, T., Raeder, K., Liu, H., Collins, N., Torn, R., & Avellano, A. (2009). The data assimilation research testbed: A community facility. *Bulletin of the American Meteorological Society*, *90*(9), 1283–1296. https://doi.org/10.1175/2009BAMS2618.1

Anderson, J. L., Hoar, T., Raeder, K., & Collins, N. (2004). Data assimilation research testbed [Software]. *UCAR/NCAR - Computational and Information Systems Laboratory (CISL)*. https://doi.org/10.5065/D6WQ0202

Baker, N. L., & Daley, R. (2000). Observation and background adjoint sensitivity in the adaptive observation-targeting problem. *Quarterly Journal of the Royal Meteorological Society*, *126*(565), 1431–1454. https://doi.org/10.1175/1520-0493(1992)120⟨0164:TEOSCO⟩2.0.CO;2

Belehaki, A., Stanislawska, I., & Lilensten, J. (2009). An overview of ionosphere—Thermosphere models available for space weather purposes. *Space Science Reviews*, *147*(3–4), 271–313. https://doi.org/10.1007/s11214-009-9510-0

Bergemann, K., & Reich, S. (2010). A modified ensemble Kalman filter. *Quarterly Journal of the Royal Meteorological Society*, *136*(651), 1636–1643. https://doi.org/10.1002/qj.672

Bowman, B., Tobiska, W. K., Marcos, F., Huang, C., Lin, C., & Burke, W. (2008). A new empirical thermospheric density model JB2008 using new solar and geomagnetic indices. In *Aiaa/aas astrodynamics Specialist Conference and Exhibit* (p. 6438). https://doi.org/10.2514/6.2008-6438

Bruinsma, S. (2015). The DTM-2013 thermosphere model. *Journal of Space Weather and Space Climate*, *5*, A1. https://doi.org/10.1051/swsc/2015001

Bruinsma, S., Sutton, E., Solomon, S., Fuller-Rowell, T., & Fedrizzi, M. (2018). Space weather modeling capabilities assessment: Neutral density for orbit determination at low Earth orbit. *Space Weather*, *16*(11), 1806–1816. https://doi.org/10.1029/2018SW002027

Burgers, G., Van Leeuwen, P. J., & Evensen, G. (1998). Analysis scheme in the ensemble Kalman filter. *Monthly Weather Review*, *126*(6), 1719–1724. https://doi.org/10.1175/1520-0493(1998)126⟨1719:ASITEK⟩2.0.CO;2

Bust, G., & Immel, T. (2020). IDA4D: Ionospheric data assimilation for the ICON mission. *Space Science Reviews*, *216*(3), 1–17. https://doi.org/10.1007/s11214-020-00648-z

Bust, G. S., Garner, T. W., & Gaussiran II, T. L. (2004). Ionospheric data assimilation three-dimensional (IDA3D): A global, multisensor, electron density specification algorithm. *Journal of Geophysical Research*, *109*(A11). https://doi.org/10.1029/2003JA010234

Cantrall, C. E., Matsuo, T., & Solomon, S. C. (2019). Upper atmosphere radiance data assimilation: A feasibility study for gold far ultraviolet observations. *Journal of Geophysical Research: Space Physics*, *124*(10), 8154–8164. https://doi.org/10.1029/2019JA026910

Chapter 7—ionosphere-thermosphere interaction. (2022). In Y. Nishimura, O. Verkhoglyadova, Y. Deng, & S.-R. Zhang (Eds.), *Cross-scale coupling and energy transfer in the magnetosphere-ionosphere-thermosphere system* (pp. 441–546). Elsevier. https://doi.org/10.1016/B978-0-12-821366-7.00003-2

Chen, C. H., Lin, C. H., Matsuo, T., Chen, W. H., Lee, I. T., Liu, J. Y., et al. (2016). Ionospheric data assimilation with thermosphere-ionosphere-electrodynamics general circulation model and GPS-TEC during geomagnetic storm conditions. *Journal of Geophysical Research: Space Physics*, *121*(6), 5708–5722. https://doi.org/10.1002/2015JA021787

Cierpik, K. M., Forbes, J. M., Miyahara, S., Miyoshi, Y., Fahrutdinova, A., Jacobi, C., et al. (2003). Longitude variability of the solar semidiurnal tide in the lower thermosphere through assimilation of ground- and space-based wind measurements. *Journal of Geophysical Research*, *108*(A5). https://doi.org/10.1029/2002JA009349

Codrescu, M. V., Fuller-Rowell, T. J., & Minter, C. F. (2004). An ensemble-type Kalman filter for neutral thermospheric composition during geomagnetic storms. *Space Weather*, *2*(11). https://doi.org/10.1029/2004SW000088

Codrescu, S. M., Codrescu, M. V., & Fedrizzi, M. (2018). An ensemble Kalman filter for the thermosphere-ionosphere. *Space Weather*, *16*(1), 57–68. https://doi.org/10.1002/2017SW001752

Datta-Barua, S., Bust, G. S., & Crowley, G. (2013). First storm-time plasma velocity estimates from high-resolution ionospheric data assimilation. *Journal of Geophysical Research: Space Physics*, *118*(11), 7458–7471. https://doi.org/10.1002/2013JA019153

De Boor, C. (1978). In *A practical guide to splines* (Vol. 27). Springer-Verlag.

Doornbos, E. (2012). *Thermospheric density and wind determination from satellite dynamics*. Springer Science & Business Media. Retrieved from http://resolver.tudelft.nl/uuid:33002be1-1498-4bec-a440-4c90ec149aea

Doornbos, E., Van Den Ijssel, J., Luhr, H., Forster, M., & Koppenwallner, G. (2010). Neutral density and crosswind determination from arbitrarily oriented multiaxis accelerometers on satellites. *Journal of Spacecraft and Rockets*, *47*(4), 580–589. https://doi.org/10.2514/1.48114

Emmert, J. (2015). Thermospheric mass density: A review. *Advances in Space Research*, *56*(5), 773–824. https://doi.org/10.1016/j.asr.2015.05.038

Evensen, G. (2003). The ensemble Kalman filter: Theoretical formulation and practical implementation. *Ocean Dynamics*, *53*(4), 343–367. https://doi.org/10.1007/s10236-003-0036-9

Evensen, G. (2009). The ensemble Kalman filter for combined state and parameter estimation. *IEEE Control Systems Magazine*, *29*(3), 83–104. https://doi.org/10.1109/MCS.2009.932223

Farchi, A., & Bocquet, M. (2019). On the efficiency of covariance localisation of the ensemble Kalman filter using augmented ensembles. *Frontiers in Applied Mathematics and Statistics*, *3*. https://doi.org/10.3389/fams.2019.00003

Fernandez-Gomez, I., Kodikara, T., Borries, C., Forootan, E., Goss, A., Schmidt, M., & Codrescu, M. V. (2022). Improving estimates of the ionosphere during geomagnetic storm conditions through assimilation of thermospheric mass density. *Earth Planets and Space*, *74*(1), 121. https://doi.org/10.1186/s40623-022-01678-3

Fesen, C., Hysell, D., Meriwether, J., Mendillo, M., Fejer, B., Roble, R., et al. (2002). Modeling the low-latitude thermosphere and ionosphere. *Journal of Atmospheric and Solar-Terrestrial Physics*, *64*(12), 1337–1349. (Equatorial Aeronomy). https://doi.org/10.1016/S1364-6826(02)00098-6

Flechtner, F., Morton, P., Watkins, M., & Webb, F. (2014). Status of the GRACE follow-on mission. In *Gravity, geoid and height systems* (pp. 117–121). Springer. https://doi.org/10.1007/978-3-319-10837-7

Forootan, E. (2014). *Statistical signal decomposition techniques for analyzing time-variable satellite gravimetry data* Doctoral dissertation. University of Bonn. Retrieved from https://hdl.handle.net/20.500.11811/1452

Forootan, E., Farzaneh, S., Kosary, M., Schmidt, M., & Schumacher, M. (2020). A simultaneous calibration and data assimilation (C/DA) to improve NRLMSISE00 using thermospheric neutral density (TND) from space-borne accelerometer measurements. *Geophysical Journal International*, *224*(2), 1096–1115. https://doi.org/10.1093/gji/ggaa507

Forootan, E., Kosary, M., Farzaneh, S., Kodikara, T., Vielberg, K., Fernandez-Gomez, I., et al. (2022). Forecasting global and multi-level thermospheric neutral density and ionospheric electron content by tuning models against satellite-based accelerometer measurements. *Scientific Reports*, *12*(1), 1–19. https://doi.org/10.1038/s41598-022-05952-y

Forsythe, V. V., Azeem, I., Blay, R., Crowley, G., Gasperini, F., Hughes, J., et al. (2021). Evaluation of the new background covariance model for the ionospheric data assimilation. *Radio Science*, *56*(8), e2021RS007286. https://doi.org/10.1029/2021RS007286

Forsythe, V. V., Azeem, I., Blay, R., Crowley, G., Makarevich, R. A., & Wu, W. (2021). Data assimilation retrieval of electron density profiles from ionosonde virtual height data. *Radio Science*, *56*(5), e2021RS007264. https://doi.org/10.1029/2021RS007264

Fuller-Rowell, T. J., & Rees, D. (1980). A three-dimensional time-dependent global model of the thermosphere. *Journal of the Atmospheric Sciences*, *37*(11), 2545–2567. https://doi.org/10.1175/1520-0469(1980)037⟨2545:ATDTDG⟩2.0.CO;2

Gaspari, G., & Cohn, S. E. (1999). Construction of correlation functions in two and three dimensions. *Quarterly Journal of the Royal Meteorological Society*, *125*(554), 723–757. https://doi.org/10.1002/qj.49712555417

Hagan, M. E., Roble, R. G., & Hackney, J. (2001). Migrating thermospheric tides. *Journal of Geophysical Research*, *106*(A7), 12739–12752. https://doi.org/10.1029/2000JA000344

Hajj, G. A., Wilson, B. D., Wang, C., Pi, X., & Rosen, I. G. (2004). Data assimilation of ground GPS total electron content into a physics-based ionospheric model by use of the Kalman filter. *Radio Science*, *39*(1), 1–17. https://doi.org/10.1029/2002RS002859

Hamill, T. M., Whitaker, J. S., & Snyder, C. (2001). Distance-dependent filtering of background error covariance estimates in an ensemble Kalman filter. *Monthly Weather Review*, *129*(11), 2776–2790. https://doi.org/10.1175/1520-0493(2001)129⟨2776:DDFOBE⟩2.0.CO;2

He, J., Yue, X., Le, H., Ren, Z., & Wan, W. (2020). Evaluation on the quasi-realistic ionospheric prediction using an ensemble Kalman filter data assimilation algorithm. *Space Weather*, *18*(3), e2019SW002410. https://doi.org/10.1029/2019SW002410

Heelis, R. A., Lowell, J. K., & Spiro, R. W. (1982). A model of the high-latitude ionospheric convection pattern. *Journal of Geophysical Research*, *87*(A8), 6339–6345. https://doi.org/10.1029/JA087iA08p06339

Houtekamer, P. L., & Zhang, F. (2016). Review of the ensemble Kalman filter for atmospheric data assimilation. *Monthly Weather Review*, *144*(12), 4489–4532. https://doi.org/10.1175/MWR-D-15-0440.1

Hsu, C.-T., Matsuo, T., Wang, W., & Liu, J.-Y. (2014). Effects of inferring unobserved thermospheric and ionospheric state variables by using an ensemble Kalman filter on global ionospheric specification and forecasting. *Journal of Geophysical Research: Space Physics*, *119*(11), 9256–9267. https://doi.org/10.1002/2014JA020390

Hsu, C.-T., Matsuo, T., Yue, X., Fang, T.-W., Fuller-Rowell, T., Ide, K., & Liu, J.-Y. (2018). Assessment of the impact of FORMOSAT-7/COSMIC-2 GNSS RO observations on midlatitude and low-latitude ionosphere specification: Observing system simulation experiments using ensemble square root filter. *Journal of Geophysical Research: Space Physics*, *123*(3), 2296–2314. https://doi.org/10.1002/2017JA025109

Huba, J. D., & Sazykin, S. (2014). Storm time ionosphere and plasmasphere structuring: Sami3-rcm simulation of the 31 march 2001 geomagnetic storm. *Geophysical Research Letters*, *41*(23), 8208–8214. https://doi.org/10.1002/2014GL062110

Jacchia, L. G. (1971). Revised static models of the thermosphere and exosphere with empirical temperature profiles SAO Special Report 332.

Jee, G., Burns, A. G., Wang, W., Solomon, S. C., Schunk, R. W., Scherliess, L., et al. (2008). Driving the ting model with GAIM electron densities: Ionospheric effects on the thermosphere. *Journal of Geophysical Research*, *113*(A3). https://doi.org/10.1029/2007JA012580

Khattatov, B., Murphy, M., Gnedin, M., Sheffel, J., Adams, J., Cruickshank, B., et al. (2005). Ionospheric nowcasting via assimilation of GPS measurements of ionospheric electron content in a global physics-based time-dependent model. *Quarterly Journal of the Royal Meteorological Society*, *131*(613), 3543–3559. https://doi.org/10.1256/qj.05.96

Kodikara, T., Zhang, K., Pedatella, N. M., & Borries, C. (2021). The impact of solar activity on forecasting the upper atmosphere via assimilation of electron density data. *Space Weather*, *19*(5), e2020SW002660. https://doi.org/10.1029/2020SW002660

Kosary, M., Farzaneh, S., Schumacher, M., & Forootan, E. (2024). Data archive accompanying assimilating space-based thermospheric neutral density (tnd) data into the tie-gcm coupled model during periods with low and high solar activity [Dataset]. *Zenodo*. https://doi.org/10.5281/zenodo.10732144

Kosary, M., Forootan, E., Farzaneh, S., & Schumacher, M. (2022). A sequential calibration approach based on the ensemble Kalman filter (C-EnKF) for forecasting total electron content (TEC). *Journal of Geodesy*, *96*(4), 29. https://doi.org/10.1007/s00190-022-01623-y

Krauss, S., Temmer, M., & Vennerstrom, S. (2018). Multiple satellite analysis of the Earth's thermosphere and interplanetary magnetic field variations due to ICME/CIR events during 2003–2015. *Journal of Geophysical Research: Space Physics*, *123*(10), 8884–8894. https://doi.org/10.1029/2018JA025778

Lee, I. T., Matsuo, T., Richmond, A. D., Liu, J. Y., Wang, W., Lin, C. H., et al. (2012). Assimilation of FORMOSAT-3/COSMIC electron density profiles into a coupled thermosphere/ionosphere model using ensemble Kalman filtering. *Journal of Geophysical Research*, *117*(A10). https://doi.org/10.1029/2012JA017700

Lei, J., Syndergaard, S., Burns, A. G., Solomon, S. C., Wang, W., Zeng, Z., et al. (2007). Comparison of COSMIC ionospheric measurements with ground-based observations and model predictions: Preliminary results. *Journal of Geophysical Research*, *112*(A7). https://doi.org/10.1029/2006JA012240

Lin, C. Y., Matsuo, T., Liu, J. Y., Lin, C. H., Tsai, H. F., & Araujo-Pradere, E. A. (2015). Ionospheric assimilation of radio occultation and ground-based GPS data using non-stationary background model error covariance. *Atmospheric Measurement Techniques*, *8*(1), 171–182. https://doi.org/10.5194/amt-8-171-2015

Liou, Y.-A., Pavelyev, A. G., Liu, S.-F., Pavelyev, A. A., Yen, N., Huang, C.-Y., & Fong, C.-J. (2007). FORMOSAT-3/COSMIC GPS radio occultation mission: Preliminary results. *IEEE Transactions on Geoscience and Remote Sensing*, *45*(11), 3813–3826. https://doi.org/10.1109/TGRS.2007.903365

Lomidze, L., Scherliess, L., & Schunk, R. W. (2015). Magnetic meridional winds in the thermosphere obtained from global assimilation of ionospheric measurements (GAIM) model. *Journal of Geophysical Research: Space Physics*, *120*(9), 8025–8044. https://doi.org/10.1002/2015JA021098

López López, P., Sutanudjaja, E. H., Schellekens, J., Sterk, G., & Bierkens, M. F. (2017). Calibration of a large-scale hydrological model using satellite-based soil moisture and evapotranspiration products. *Hydrology and Earth System Sciences*, *21*(6), 3125–3144. https://doi.org/10.5194/hess-21-3125-2017

Lorenc, A. C. (2003). The potential of the ensemble Kalman filter for NWP—A comparison with 4D-Var. *Quarterly Journal of the Royal Meteorological Society*, *129*(595), 3183–3203. https://doi.org/10.1256/qj.02.132

Matsuo, T., & Araujo-Pradere, E. A. (2011). Role of thermosphere-ionosphere coupling in a global ionospheric specification. *Radio Science*, *46*(06), 1–7. https://doi.org/10.1029/2010RS004576

Matsuo, T., Lee, I.-T., & Anderson, J. L. (2013). Thermospheric mass density specification using an ensemble Kalman filter. *Journal of Geophysical Research: Space Physics*, *118*(3), 1339–1350. https://doi.org/10.1002/jgra.50162

Maute, A. (2017). Thermosphere-ionosphere-electrodynamics general circulation model for the ionospheric connection explorer: TIEGCM-ICON. *Space Science Reviews*, *212*(1), 523–551. https://doi.org/10.1007/s11214-017-0330-3

Mehta, P., & Linares, R. (2017). A methodology for reduced order modeling and calibration of the upper atmosphere. *Space Weather*, *15*(10), 1270–1287. https://doi.org/10.1002/2017SW001642

Mehta, P., & Linares, R. (2018). A new transformative framework for data assimilation and calibration of physical ionosphere-thermosphere models. *Space Weather*, *16*(8), 1086–1100. https://doi.org/10.1029/2018SW001875

Mehta, P. M., Linares, R., & Sutton, E. K. (2019). Data-driven inference of thermosphere composition during solar minimum conditions. *Space Weather*, *17*(9), 1364–1379. https://doi.org/10.1029/2019SW002264

Mehta, P. M., Walker, A. C., Sutton, E. K., & Godinez, H. C. (2017). New density estimates derived using accelerometers on board the CHAMP and GRACE satellites. *Space Weather*, *15*(4), 558–576. https://doi.org/10.1002/2016SW001562

Millward, G. H., Müller-Wodarg, I. C. F., Aylward, A. D., Fuller-Rowell, T. J., Richmond, A. D., & Moffett, R. J. (2001). An investigation into the influence of tidal forcing on f region equatorial vertical ion drift using a global ionosphere-thermosphere model with coupled electrodynamics. *Journal of Geophysical Research*, *106*(A11), 24733–24744. https://doi.org/10.1029/2000JA000342

Miyoshi, Y., Fujiwara, H., Jin, H., Shinagawa, H., Liu, H., & Terada, K. (2011). Model study on the formation of the equatorial mass density anomaly in the thermosphere. *Journal of Geophysical Research*, *116*(A5). https://doi.org/10.1029/2010JA016315

Palmroth, M., Grandin, M., Sarris, T., Doornbos, E., Tourgaidis, S., Aikio, A., et al. (2021). Lower-thermosphere-ionosphere (LTI) quantities: Current status of measuring techniques and models. *Annales Geophysicae*, *39*(1), 189–237. https://doi.org/10.5194/angeo-39-189-2021

Pedatella, N., Yue, X., & Schreiner, W. (2015). Comparison between GPS radio occultation electron densities and in situ satellite observations. *Radio Science*, *50*(6), 518–525. https://doi.org/10.1002/2015RS005677

Pedatella, N. M., Anderson, J. L., Chen, C. H., Raeder, K., Liu, J., Liu, H.-L., & Lin, C. H. (2020). Assimilation of ionosphere observations in the whole atmosphere community climate model with thermosphere-ionosphere extension (WACCMX). *Journal of Geophysical Research: Space Physics*, *125*(9), e2020JA028251. https://doi.org/10.1029/2020JA028251

Pi, X., Wang, C., Hajj, G. A., Rosen, G., Wilson, B. D., & Bailey, G. J. (2003). Estimation of e × b drift using a global assimilative ionospheric model: An observation system simulation experiment. *Journal of Geophysical Research*, *108*(A2). https://doi.org/10.1029/2001JA009235

Picone, J., Hedin, A., Drob, D. P., & Aikin, A. (2002). Nrlmsise-00 empirical model of the atmosphere: Statistical comparisons and scientific issues. *Journal of Geophysical Research*, *107*(A12), 1468. https://doi.org/10.1029/2002JA009430

Preisendorfer, R. (1988). *Principal component analysis in meteorology and oceanography*. Elsevier.

Qian, L., Burns, A. G., Emery, B. A., Foster, B., Lu, G., Maute, A., et al. (2014). The NCAR TIE-GCM: A community model of the coupled thermosphere/ionosphere system. *Modeling the Ionosphere-Thermosphere System*, *201*, 73–83. https://doi.org/10.1002/9781118704417.ch7

Qian, L., Burns, A. G., Solomon, S. C., & Chamberlin, P. C. (2012). Solar flare impacts on ionospheric electrodyamics. *Geophysical Research Letters*, *39*(6). https://doi.org/10.1029/2012GL051102

Qian, L., & Solomon, S. C. (2012). Thermospheric density: An overview of temporal and spatial variations. *Space Science Reviews*, *168*(1), 147–173. https://doi.org/10.1007/s11214-011-9810-z

Qian, L., Solomon, S. C., & Kane, T. J. (2009). Seasonal variation of thermospheric density and composition. *Journal of Geophysical Research*, *114*(A1). https://doi.org/10.1029/2008JA013643

Reigber, C., Lühr, H., & Schwintzer, P. (2002). CHAMP mission status. *Advances in Space Research*, *30*(2), 129–134. https://doi.org/10.1016/S0273-1177(02)00276-4

Ren, D., & Lei, J. (2020). Evaluation of physics-based data assimilation system driven by neutral density data from a single satellite. *Space Weather*, *18*(8), e2020SW002504. https://doi.org/10.1029/2020SW002504

Richmond, A. D., Ridley, E. C., & Roble, R. G. (1992). A thermosphere/ionosphere general circulation model with coupled electrodynamics. *Geophysical Research Letters*, *19*(6), 601–604. https://doi.org/10.1029/92GL00401

Ridley, A., Deng, Y., & Toth, G. (2006). The global ionosphere-thermosphere model. *Journal of Atmospheric and Solar-Terrestrial Physics*, *68*(8), 839–864. https://doi.org/10.1016/j.jastp.2006.01.008

Roble, R. G., & Ridley, E. C. (1994). A thermosphere-ionosphere-mesosphere-electrodynamics general circulation model TIME-GCM: Equinox solar cycle minimum simulations (30–500 km). *Geophysical Research Letters*, *21*(6), 417–420. https://doi.org/10.1029/93GL03391

Ruan, H., Lei, J., Dou, X., Liu, S., & Aa, E. (2018). An exospheric temperature model based on CHAMP observations and TIEGCM simulations. *Space Weather*, *16*(2), 147–156. https://doi.org/10.1002/2017SW001759

Scherliess, L., Schunk, R. W., Sojka, J. J., & Thompson, D. C. (2004). Development of a physics-based reduced state Kalman filter for the ionosphere. *Radio Science*, *39*(1), 1–12. https://doi.org/10.1029/2002RS002797

Scherliess, L., Schunk, R. W., Sojka, J. J., Thompson, D. C., & Zhu, L. (2006). Utah state University global assimilation of ionospheric measurements Gauss-Markov Kalman filter model of the ionosphere: Model description and validation. *Journal of Geophysical Research*, *111*(A11). https://doi.org/10.1029/2006JA011712

Scherliess, L., Thompson, D. C., & Schunk, R. W. (2009). Ionospheric dynamics and drivers obtained from a physics-based data assimilation model. *Radio Science*, *44*(01), 1–8. https://doi.org/10.1029/2008RS004068

Shim, J. S., Kuznetsova, M., Rastätter, L., Bilitza, D., Butala, M., Codrescu, M., et al. (2014). Systematic evaluation of ionosphere/thermosphere (IT) models. In *Modeling the ionosphere–thermosphere system* (pp. 145–160). American Geophysical Union (AGU). https://doi.org/10.1002/9781118704417.ch13

Siemes, C., Borries, C., Bruinsma, S., Fernandez-Gomez, I., Hładczuk, N., den IJssel, J., et al. (2023). New thermosphere neutral mass density and crosswind datasets from CHAMP, GRACE, and GRACE-FO. *Journal of Space Weather and Space Climate*, *13*, 16. https://doi.org/10.1051/swsc/2023014

Solomon, S. C., Qian, L., Didkovsky, L. V., Viereck, R. A., & Woods, T. N. (2011). Causes of low thermospheric density during the 2007–2009 solar minimum. *Journal of Geophysical Research*, *116*(A2). https://doi.org/10.1029/2011JA016508

Sutton, E. (2011). Accelerometer-derived atmospheric densities from the CHAMP and GRACE satellites: Version 2.3. AFRL Technical Memo, DTIC# ADA537198.

Sutton, E. (2018). A new method of physics-based data assimilation for the quiet and disturbed thermosphere. *Space Weather*, *16*(6), 736–753. https://doi.org/10.1002/2017SW001785

Sutton, E., Nerem, R., & Forbes, J. (2007). Density and winds in the thermosphere deduced from accelerometer data. *Journal of Spacecraft and Rockets*, *44*(6), 1210–1219. https://doi.org/10.2514/1.28641

Tapley, B. D., Bettadpur, S., Ries, J. C., Thompson, P. F., & Watkins, M. M. (2004). GRACE measurements of mass variability in the Earth system. *Science*, *305*(5683), 503–505. https://doi.org/10.1126/science.1099192

Vallado, D. A. (2004). *Fundamentals of astrodynamics and applications* second printing. Microcosm, El Segundo.

Vallado, D. A., & Finkleman, D. (2014). A critical assessment of satellite drag and atmospheric density modeling. *Acta Astronautica*, *95*, 141–165. https://doi.org/10.1016/j.actaastro.2013.10.005

Van Den IJssel, J., Doornbos, E., Iorfida, E., March, G., Siemes, C., & Montenbruck, O. (2020). Thermosphere densities derived from Swarm GPS observations. *Advances in Space Research*, *65*(7), 1758–1771. https://doi.org/10.1016/j.asr.2020.01.004

Vielberg, K., Forootan, E., Lück, C., Löcher, A., Kusche, J., & Börger, K. (2018). Comparison of accelerometer data calibration methods used in thermospheric neutral density estimation. *Annales Geophysicae*, *36*(3), 761–779. https://doi.org/10.5194/angeo-36-761-2018

Vielberg, K., Lück, C., Corbin, A., Forootan, E., Löcher, A., & Kusche, J. (2021). TND-IGG RL01: Thermospheric neutral density from accelerometer measurements of GRACE, CHAMP and Swarm [Dataset]. *PANGAEA*. https://doi.org/10.1594/PANGAEA.931347

Visser, P., Doornbos, E., van den IJssel, J., & Da Encarnação, J. T. (2013). Thermospheric density and wind retrieval from Swarm observations. *Earth Planets and Space*, *65*(11), 1319–1331. https://doi.org/10.5047/eps.2013.08.003

Wang, C., Hajj, G., Pi, X., Rosen, I. G., & Wilson, B. (2004). Development of the global assimilative ionospheric model. *Radio Science*, *39*(1), 1–11. https://doi.org/10.1029/2002RS002854

Wang, W., Wiltberger, M., Burns, A., Solomon, S., Killeen, T., Maruyama, N., & Lyon, J. (2004). Initial results from the coupled magnetosphere–ionosphere–thermosphere model: Thermosphere–ionosphere responses. *Journal of Atmospheric and Solar-Terrestrial Physics*, *66*(15), 1425–1441. https://doi.org/10.1016/j.jastp.2004.04.008

Weimer, D. R. (2005). Improved ionospheric electrodynamic models and application to calculating joule heating rates. *Journal of Geophysical Research*, *110*(A5). https://doi.org/10.1029/2004JA010884

Weimer, D. R., Mehta, P. M., Tobiska, W. K., Doornbos, E., Mlynczak, M. G., Drob, D. P., & Emmert, J. T. (2020). Improving neutral density predictions using exospheric temperatures calculated on a geodesic, polyhedral grid. *Space Weather*, *18*(1), e2019SW002355. https://doi.org/10.1029/2019SW002355

Yang, K.-F., Chu, Y.-H., Su, C.-L., Ko, H.-T., & Wang, C.-Y. (2009). An examination of FORMOSAT-3/COSMIC ionospheric electron density profile: Data quality criteria and comparisons with the IRI model. *Terrestrial, Atmospheric and Oceanic Sciences*, *20*(1), 193. https://doi.org/10.3319/TAO.2007.10.05.01(F3C)

Yue, J., Jian, Y., Wang, W., Meier, R., Burns, A., Qian, L., et al. (2019). Annual and semiannual oscillations of thermospheric composition in TIMED/GUVI Limb measurements. *Journal of Geophysical Research: Space Physics*, *124*(4), 3067–3082. https://doi.org/10.1029/2019JA026544

Yue, X., Schreiner, W. S., Rocken, C., & Kuo, Y.-H. (2011). Evaluation of the orbit altitude electron density estimation and its effect on the Abel inversion from radio occultation measurements. *Radio Science*, *46*(1). https://doi.org/10.1029/2010RS004514

Zesta, E., & Huang, C. Y. (2016). Satellite orbital drag. *Space Weather Fundamentals*, 329–351. https://doi.org/10.1201/9781315368474-20

Zhang, Y., & Paxton, L. (2008). An empirical kp-dependent global auroral model based on TIMED/GUVI FUV data. *Journal of Atmospheric and Solar-Terrestrial Physics*, *70*(8), 1231–1242. https://doi.org/10.1016/j.jastp.2008.03.008

Zhu, J., Zheng, F., & Li, X. (2011). A new localization implementation scheme for ensemble data assimilation of non-local observations. *Tellus A: Dynamic Meteorology and Oceanography*, *63*(2), 244–255. https://doi.org/10.1111/j.1600-0870.2010.00486.x